Cell Reports

Article

Parvalbumin interneuron dendrites enhance gamma oscillations

Graphical abstract

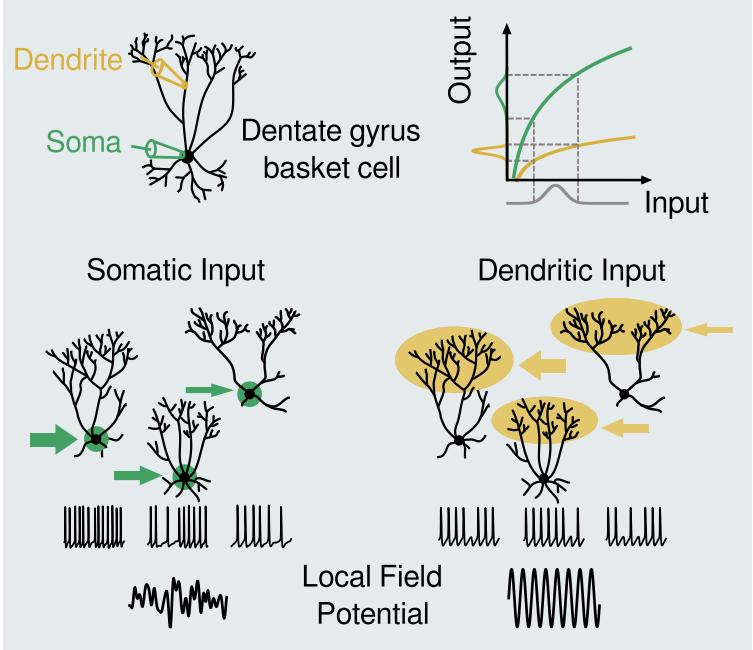

Highlights

- The gain of the input-output relationship of PV+ basket cell dendrites is very low
- The low gain enhances spike synchrony in the gamma (40–110 Hz) frequency range
- In highly heterogeneous networks, the low gain is key to preserve gamma oscillations

Authors

Birgit Kriener, Hua Hu, Koen Vervaeke

Correspondence

koenv@medisin.uio.no

In brief

By performing *in vitro* patch-clamp recordings from parvalbumin-expressing basket cell dendrites, Kriener et al. report that the gain of the dendritic input-output relationship is exceptionally low. Simulations indicate that this dendritic feature is key to enhancing the coherence of network activity in the gamma frequency range.

Kriener et al., 2022, Cell Reports *39*, 110948
June 14, 2022
https://doi.org/10.1016/j.celrep.2022.110948

CellPress

Cell Reports

CellPress
OPEN ACCESS

Article

Parvalbumin interneuron dendrites enhance gamma oscillations

Birgit Kriener,[1] Hua Hu,[1] and Koen Vervaeke[1,2,*]
[1]Institute of Basic Medical Sciences, Section of Physiology, University of Oslo, Oslo, Norway
[2]Lead contact
*Correspondence: koenv@medisin.uio.no
https://doi.org/10.1016/j.celrep.2022.110948

SUMMARY

Dendrites are essential determinants of the input-output relationship of single neurons, but their role in network computations is not well understood. Here, we use a combination of dendritic patch-clamp recordings and *in silico* modeling to determine how dendrites of parvalbumin (PV)-expressing basket cells contribute to network oscillations in the gamma frequency band. Simultaneous soma-dendrite recordings from PV basket cells in the dentate gyrus reveal that the slope, or gain, of the dendritic input-output relationship is exceptionally low, thereby reducing the cell's sensitivity to changes in its input. By simulating gamma oscillations in detailed network models, we demonstrate that the low gain is key to increase spike synchrony in PV basket cell assemblies when cells are driven by spatially and temporally heterogeneous synaptic inputs. These results highlight the role of inhibitory neuron dendrites in synchronized network oscillations.

INTRODUCTION

Network oscillations in the gamma frequency band (40–110 Hz) are a prominent circuit feature of many brain areas and likely support a variety of cognitive processes such as perception (Gray et al., 1989), attentional selection (Fries et al., 2001), and memory (Lisman and Idiart, 1995; Lundqvist et al., 2016). The important roles for gamma oscillations have triggered numerous studies investigating how they are generated. These show that parvalbumin-expressing inhibitory neurons, which form axonal "baskets" around the soma of target neurons (hence called parvalbumin [PV] basket cells; Hu et al., 2014), play a central role in the cortex (Cardin et al., 2009; Fuchs et al., 2007; Sohal et al., 2009). Although previous studies have identified a number of synaptic mechanisms in basket cells that seem optimal to generate gamma oscillations (Bartos et al., 2001, 2002, 2007; Cornford et al., 2019; Erisir et al., 1999; Fisahn et al., 1998; Hormuzdi et al., 2001; Kopell and Ermentrout, 2004; Pike et al., 2000; Strüber et al., 2015; Vida et al., 2006; Whittington et al., 1995), the dendritic properties that allow PV basket cells to transform synaptic inputs into synchronous output firing remain elusive.

Spike synchrony in an ensemble of inhibitory interneurons is a key mechanism for generating network oscillations (Bartos et al., 2007; Buzsáki and Wang, 2012). In the simplest of models, when a sufficiently large number of inhibitory neurons fire within in a small time window, they generate a pronounced inhibitory conductance in the network. If the excitatory input drive is homogeneous across cells, neurons will escape inhibition together and fire subsequently at the same time, leading to synchronous activity (Bartos et al., 2007; Buzsáki and Wang, 2012). However, when the excitatory drive varies from neuron to neuron, cells will fire at different rates and escape the common rhythm, and synchrony is lost (Wang, 2010; Wang and Buzsáki, 1996). In biological networks, a plethora of heterogeneities enhance spike-rate variability (Softky and Koch, 1993). Each cell, even of the same type, has a different excitability and morphology, and spatially distributed cells receive different amounts of excitation (spatial heterogeneity), which also fluctuates rapidly over time (temporal heterogeneity) (Calvin and Stevens, 1967; Destexhe et al., 2003). These different forms of heterogeneity have been a long-standing challenge of network models studying neural synchrony (Bartos et al., 2001, 2002, 2007; Moca et al., 2012; Neltner et al., 2000; Tiesinga and José, 2000; Tikidji-Hamburyan et al., 2015; Tort et al., 2007; Vida et al., 2006; Wang and Buzsáki, 1996; White et al., 1998).

The biophysical properties of PV basket cells further exacerbate this problem. How neurons integrate sustained excitatory synaptic input and transform it into an output firing rate is captured by their input-output (I-O) relationship (Silver, 2010). This is typically measured by injecting current in the soma and measuring spike frequency. In the case of PV basket cells, the slope, or gain, of the I-O relationship is about ten times steeper compared with cortical principal neurons (Goldberg et al., 2008). A high gain makes neurons more sensitive to changes in their input. Therefore, in an ensemble of PV basket cells that all receive different amounts of input, cells will spike at dramatically different rates, making it challenging to synchronize (illustrated in Figure 1A).

Previous work on gamma oscillations only performed network simulations using so-called "point-neuron" models that disregard the dendritic morphology. However, we hypothesized that

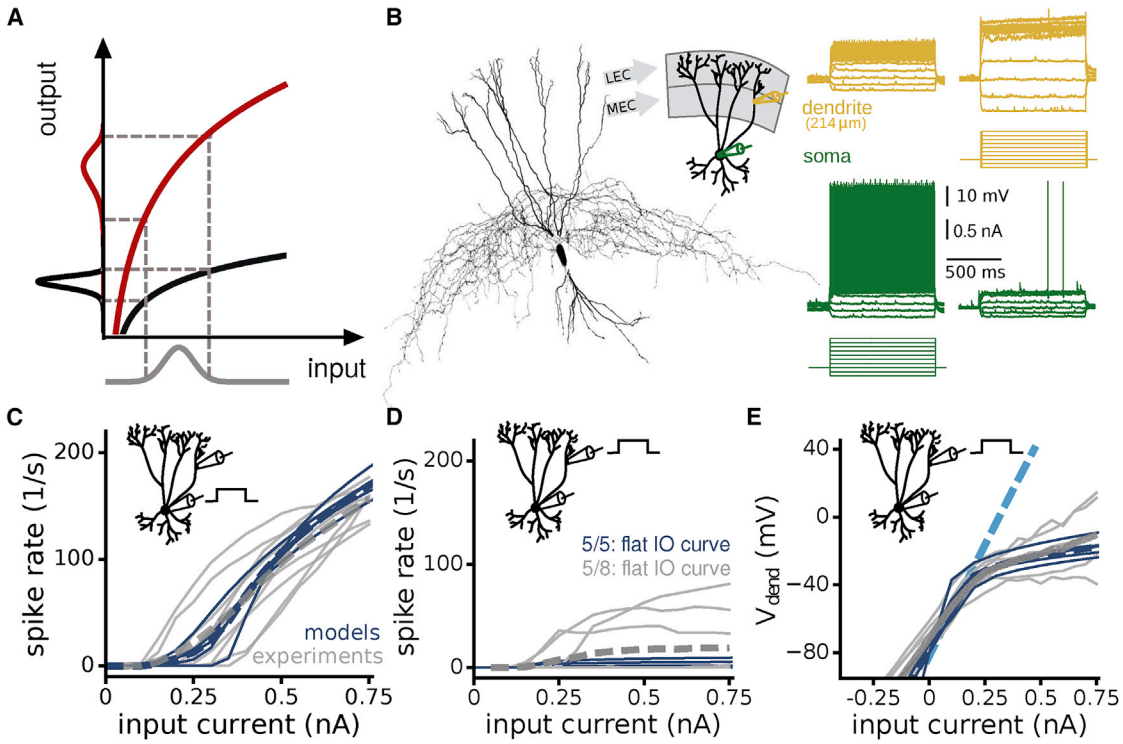

Figure 1. Dendritic input results in a lower I-O gain compared with somatic input

(A) A steeper hypothetical input-output (I-O) relationship maps the same input distribution to a broader output firing-rate distribution.

(B) Example of a dual soma-dendritic patch-clamp recording of a parvalbumin (PV)-expressing basket cell in the dentate gyrus. Cartoon shows the recording configuration and the input from the lateral and the medial entorhinal cortex (LEC and MEC, respectively). Membrane potential traces show soma and dendrite responses to current injections in either the soma (left) or the dendrite (right). Inset, example of a reconstructed morphology of a PV basket cell used for computer simulations. Scale bars apply to soma and dendrite recordings.

(C) I-O relationships when injecting current steps in the soma. Gray lines, individual experiments (n = 8 cells); blue lines, individual models (n = 5); dashed thick lines, averages.

(D) I-O relationships when injecting current steps in the dendrite. Average dendritic recording distance is 240 ± 7 µm (n = 8 cells) and 230 µm from the soma (n = 5 models). In 5/8 experiments and 5/5 models, cells fired only a few or no spikes, resulting in near-flat I-O relationships.

(E) Dendritic membrane potential in response to current steps injected in the dendrite (n = 6 cells, n = 5 models). Light blue dashed line is the average dendritic membrane potential when no voltage-dependent K^+ channels are present on the model dendrites.

PV basket cell dendrites are key for enhancing the robustness of gamma oscillations in heterogeneous networks. We made simultaneous whole-cell recordings from the dendrites and soma of PV basket cells in the dentate gyrus of the rat hippocampus, a circuit that generates prominent gamma oscillations (Bragin et al., 1995; Csicsvari et al., 2003; Towers et al., 2002). We found that, compared with the steep I-O relationship measured from the soma, the gain of the dendritic I-O relationship is scaled down. Therefore, PV basket cells are far less sensitive to different amounts of input than previously thought (Wang and Buzsáki, 1996). Furthermore, PV basket cell dendrites reduce the amplitude of fast-fluctuating synaptic responses, reducing interspike interval variability. We used anatomically detailed network models to show that PV basket cell dendrites indeed dramatically increase the robustness of gamma oscillations in a wide variety of network architectures. Closer examination of the underlying biophysical mechanisms revealed that the high-threshold and fast-activating K^+ currents in the dendrites (Hu et al., 2010) act to dampen heterogeneities and thereby enhance spike synchrony.

RESULTS

Dendritic input results in a lower I-O gain compared with somatic input

To compare the I-O relationship of soma-driven and dendrite-driven output firing in PV basket cells, we made dual whole-cell recordings from the soma and dendrites using confocal-microscope-guided patching (Hu et al., 2010). We targeted the dendrites in the middle and outer third of the molecular layer where these cells receive inputs from the medial and lateral entorhinal cortex, respectively (Amaral et al., 2007) (Figure 1B, range: 214–262 µm from the soma; 240 ± 7 µm, n = 8 cells). Current injections of increasing amplitude in the soma increased the spike frequency rapidly, leading to a steep I-O relationship (Figure 1C, gain = 380 ± 24 Hz nA^{-1}). In stark contrast, current injection in the dendrites triggered no, or low-frequency, spiking, resulting in a nearly flat average I-O relationship (Figure 1D). Inspection of the dendritic membrane potential revealed that responses to local current injection were linear up to ~−30 mV but then became sub-linear, making it increasingly hard to drive

the cell to fire (Figure 1E, and example in 1B). These data show that, compared with the soma, the gain of the dendritic I-O relationship is scaled down.

Previous work has characterized the biophysical properties of PV basket cells, such as the passive electrical membrane properties and ion-channel distributions (Hu and Jonas, 2014; Hu et al., 2010, 2014; Nörenberg et al., 2010). To test whether these known properties can account for the low I-O gain, we used a computational approach. We simulated the I-O relationship using five anatomically detailed PV basket cell models that included dendrites and the axon (examples in Figures 1B and S1A; see STAR Methods). The only voltage-dependent conductance we inserted in the dendrites was a high-threshold and fast-activating K^+ channel that is a hallmark of PV basket cells in the dentate gyrus (Hu et al., 2010). These models recapitulated the fast-spiking phenotype, the strong attenuation of backpropagating action potentials (Hu et al., 2010), and the steep soma I-O relationship (Figures 1C, S1B, and S1C, gain = 397 ± 40 Hz nA^{-1}, n = 5 models). Consistent with the majority of experiments, injecting current into the distal dendrites produced a nearly flat I-O relationship (Figures 1D, S1B, and S1C, distance = 230 μm from the soma). Furthermore, the models recapitulated the sub-linear increase of the dendritic membrane potential, which was dependent on the dendritic K^+ channels (Figure 1E). Whether the dendritic K^+ channels can also explain the dendritic I-O relationship will be addressed below. In summary, the PV basket cell models capture the essential I-O properties that we measured experimentally, and collectively, these data show that the dendrite-driven I-O relationship has a lower gain compared with soma-driven output firing.

Distributed dendritic input results in a lower I-O gain and more regular spiking

In vivo, PV basket cells likely receive both clustered and spatially distributed inputs on the dendritic tree. Dual soma-dendritic patch-clamp recordings, however, can only mimic clustered dendritic inputs. Therefore, to examine how distributed inputs affect the I-O relationship, we used the PV basket cell models. To perform these simulations, we needed to verify that the models could reproduce some of the most elementary properties of dendritic integration such as the kinetics and the attenuation of excitatory synaptic potentials (EPSPs) along the dendrites. Using dual soma-dendrite recordings, we analyzed the forward propagation of miniature EPSPs generated near the dendritic pipette (Figure 2A). The amplitude of dendritic EPSPs increased with distance from the soma, while their amplitude at the soma decreased (Figure 2B, n = 5 cells). Fitting the dendrite-to-soma attenuation with a single exponential-decay function resulted in an attenuation constant of 84 μm, which is similar to the value predicted by our models (74 ± 19 μm, n = 5 models, Figure 2C).

Having validated the PV basket cell models, we next simulated the I-O relationship for distributed synaptic inputs. We randomly positioned excitatory synapses on the outer two-thirds of the dendrites (>120 μm from the soma) or within 50 μm from the soma (Figure 2D). Simulating sustained inputs revealed that the gain of the I-O relationship for dendritic drive was again lower than for somatic drive (Figure 2D).

In addition, we observed that the dendrite-driven output firing was also more regular, as illustrated by a narrower distribution of interspike intervals (Figure 2E), a property that may help spike synchronization between PV basket cells. Quantifying the interspike interval variability by the coefficient of variation (CV; the ratio of the standard deviation to the mean) showed that dendrite-driven firing was more regular across the entire spike-frequency range (Figure 2F). We hypothesized that this was due to the strong EPSP attenuation along the dendrites (Figure 2B). Because distal dendritic EPSPs are small when arriving at the soma compared with proximal EPSPs (Figure 2A), the membrane-potential fluctuations are also smaller, leading to more regular spiking. To test this, we examined the standard deviation of the membrane potential along the dendrites during dendritic stimulation (Figure 2G). These data show that, indeed, during sustained dendritic input, the membrane-potential fluctuations are small near the soma.

In summary, these data suggest that PV basket cell dendrites may enhance gamma synchrony in two ways. First, the low gain of the dendritic I-O relationship will reduce the sensitivity of the PV basket cell output to different amounts of input, and second, the smaller membrane-potential fluctuations at the soma, evident in the more regular spiking, may facilitate spike synchronization between PV basket cells.

PV basket cell dendrites make gamma synchrony more robust to heterogeneities

To test whether PV basket cell dendrites enhance gamma synchrony in heterogeneous networks, we performed network simulations using the reconstructed PV basket cells coupled with inhibitory synapses based on empirical data (Bartos et al., 2002) (Figure 3A; see STAR Methods). We included two forms of heterogeneity: (1) each PV basket cell received a different amount of synaptic input to create spatial heterogeneity (so-called "input heterogeneity"), and (2) the input consisted of noisy Poisson trains of synaptic conductances to create temporal heterogeneity. Each cell in the network received a mean input rate taken from a normal distribution with a mean μ and standard deviation σ. We could then increase the spatial heterogeneity in the network by increasing the width of this distribution (that is, the ratio of $\sigma/\mu \times 100$ [%]). In homogenous networks (0% input heterogeneity), spike synchrony in the gamma frequency range emerged rapidly in both soma- and dendrite-driven networks (Figure 3B). However, when we increased the input heterogeneity, dendrite-driven neurons fired more synchronously (Figure 3B, compare raster plots).

The amplitude of the excitatory drive and the strength of inhibitory connections are critical determinants of the spike rates, oscillation frequency, and synchrony; therefore, we examined how they affect the results (Figure 3C). To quantify network synchrony, we defined the synchrony index, which is 1 for perfect spike synchrony and approaches 0 when the network is fully desynchronized (see STAR Methods). For soma-driven networks, increasing the input heterogeneity to 40% reduced the synchrony index for a broad range of excitation and connection strengths (Figure 3C, bottom row). In stark contrast, the dendrite-driven networks maintained a high synchrony index (Figure 3C). To summarize the relationship

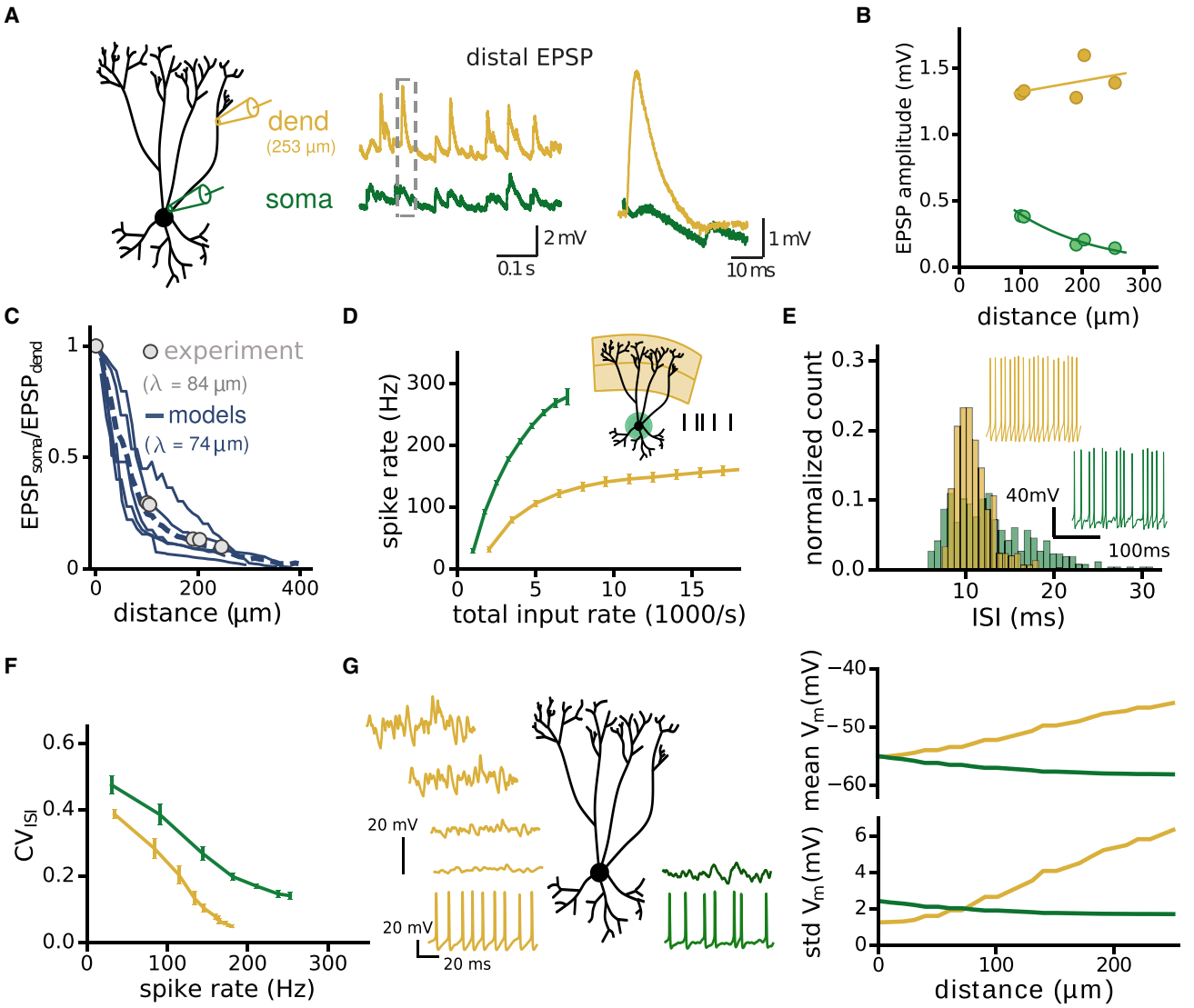

Figure 2. Distributed dendritic inputs result in a lower I-O gain and more regular spiking

(A) Cartoon shows the recording configuration. Membrane-potential traces show miniature EPSPs. We used the fast-rising slope (<0.5 ms) to determine which EPSPs originate close to the recording pipette.

(B) Mean miniature EPSP amplitude of all cells, plotted as a function of input distance from the soma, for both dendritic (orange) and somatic recordings (green, n = 5 cells, lines are least-square fits).

(C) Miniature EPSP amplitude attenuation during the propagation from the dendrites to the soma. Gray data points, experiments (n = 5 cells); blue lines, model predictions (n = 5 models); blue dashed line, average model prediction. Data and average model prediction were fitted with a single exponential decay function ($e^{-x/\lambda}$, with attenuation constant λ).

(D) I-O relationships of PV basket cell models using perisomatic (green) or distributed dendritic inputs (orange, n = 5 models, mean ± SEM, 10 simulations). Cartoon shows the synaptic input locations. Perisomatic: 50 synapses ≤ 50 µm from the soma. Dendritic: 100 synapses ≥ 120 µm from the soma. Black ticks illustrate a Poisson train of synaptic inputs. Synapses were randomly distributed. Total input rate is the number of synapses × the rate per synapse. The number of synapses was fixed, and we varied only the rate per synapse.

(E) Insets, example spike trains from the data in (D). Normalized count histograms show the interspike intervals (ISIs) of the example spike trains.

(F) ISI irregularity quantified by the coefficient of variation (CV) as a function of output spike rate (based on the data in D).

(G) Membrane-potential traces along the dendrites and the soma when the input is dendritic (orange) or perisomatic (green). For dendritic input, membrane-potential fluctuations attenuate towards the soma, leading to more regular spiking. Right panels show the mean and standard deviation of the membrane potential as a function of distance to soma. The amount of input was adjusted to achieve the same mean depolarization of the soma. Na^+ channels were blocked to prevent action potentials.

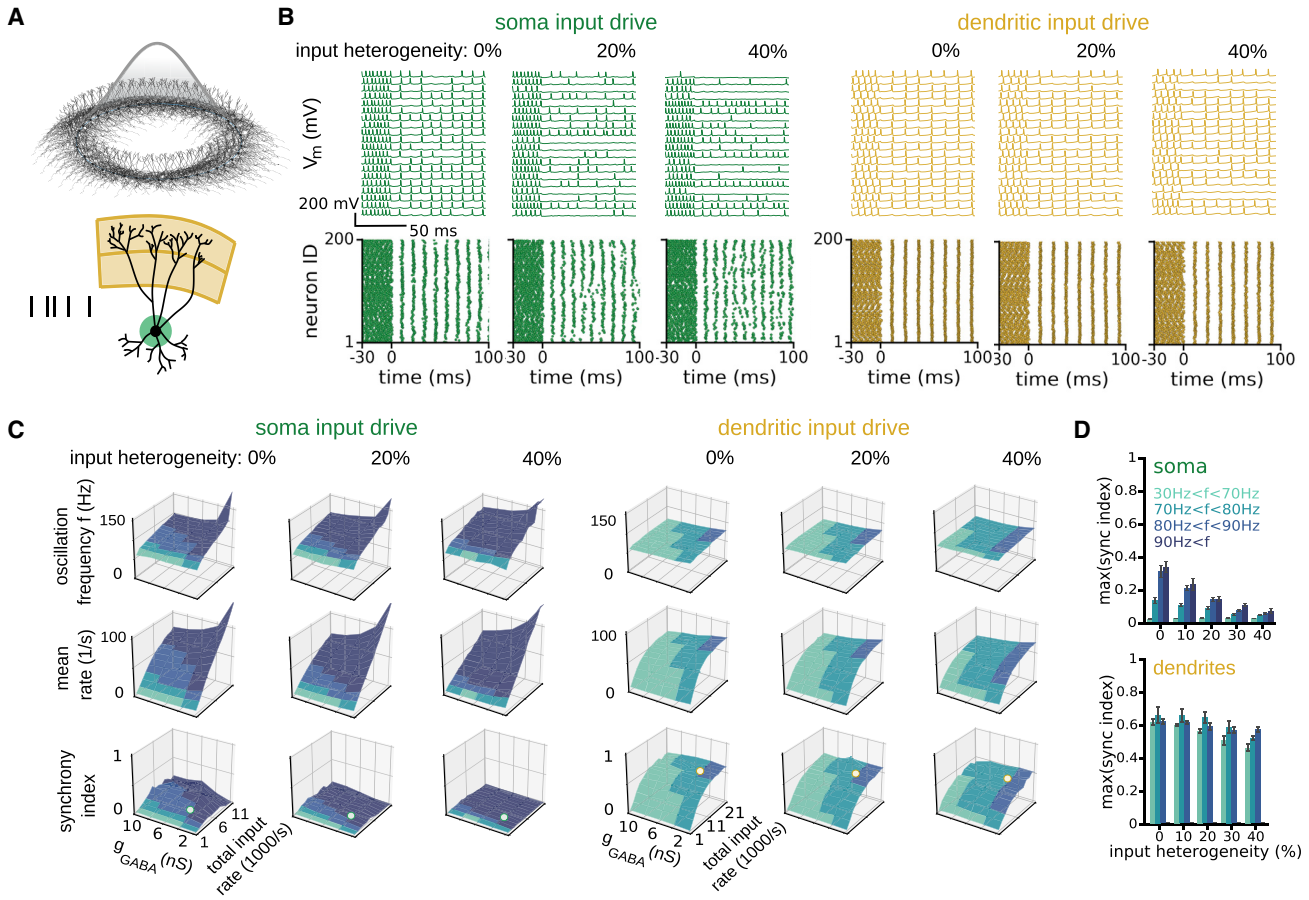

Figure 3. PV basket cell dendrites make gamma synchrony more robust to input heterogeneity

(A) Ring network of 200 PV basket cell models with a reconstructed morphology, symbolically arranged along a ring to illustrate a network with local inhibitory connections. Cells are randomly coupled by inhibitory synapses following a Gaussian connection probability (gray curve). Cartoon shows the synaptic input locations. 50 synapses $\leq$ 50 μm from the soma (green); 100 synapses $\geq$ 120 μm from soma (orange).

(B) PV basket cell activity in networks driven by perisomatic (green) or dendritic (orange) excitation. Input heterogeneity increases from left to right. Top row, example membrane-potential traces showing spikes from 20 random cells. Bottom row, raster plots of all 200 PV basket cells in the network. Network starts uncoupled, and inhibitory synapses activate at t = 0 ms.

(C) Network oscillation frequency (top row), mean spike rate (middle row), and synchrony index (bottom row) as a function of total input rate and the strength of inhibitory conductance (gGABA). The surface colors show the oscillation-frequency range (see color legend in D). White dots on the synchrony index correspond to the examples in (B).

(D) The maximum synchrony index per frequency band, as a function of input heterogeneity for perisomatic and dendritic input (based on data in C, mean ± SEM, 5 network instantiations).

between synchrony index and heterogeneity for different gamma frequency bands, we divided the gamma spectrum into smaller frequency bands and calculated the maximum synchrony index for each band (Figure 3D). These data show that regardless of the gamma frequency range, dendrite-driven networks are far more tolerant to heterogeneities. Even increasing the input heterogeneity to 100% caused only a small reduction in network synchrony (Figure S2A). Furthermore, dendrite-driven networks synchronized robustly even when the strength of inhibitory connections was an order of magnitude less compared with previous influential models (Vida et al., 2006) (see side-by-side comparison in Figures S2A–S2C). Finally, we found similar results regardless of which PV basket cell model we used for building networks, illustrating that the results do not depend on a specific cell morphology or specific biophysical properties (Figure S2D).

Notably, we observed that network synchrony in dendrite-driven networks was also higher in homogeneous networks in which all cells receive the same input (Figure 3D, 0% input heterogeneity case). Therefore, we hypothesized that the dendrites also reduced temporal heterogeneities by reducing the amplitude of the membrane potential fluctuations at the soma (see Figure 2G). This could facilitate spike synchrony. To test this, we substituted the Poisson synaptic inputs with tonic input currents to produce noiseless excitation (Figure S3). Indeed, synchrony in soma- and dendrite-driven networks was now similar (Figure 3D, 0% input heterogeneity case). Altogether, these data show that both spatial and temporal heterogeneities are

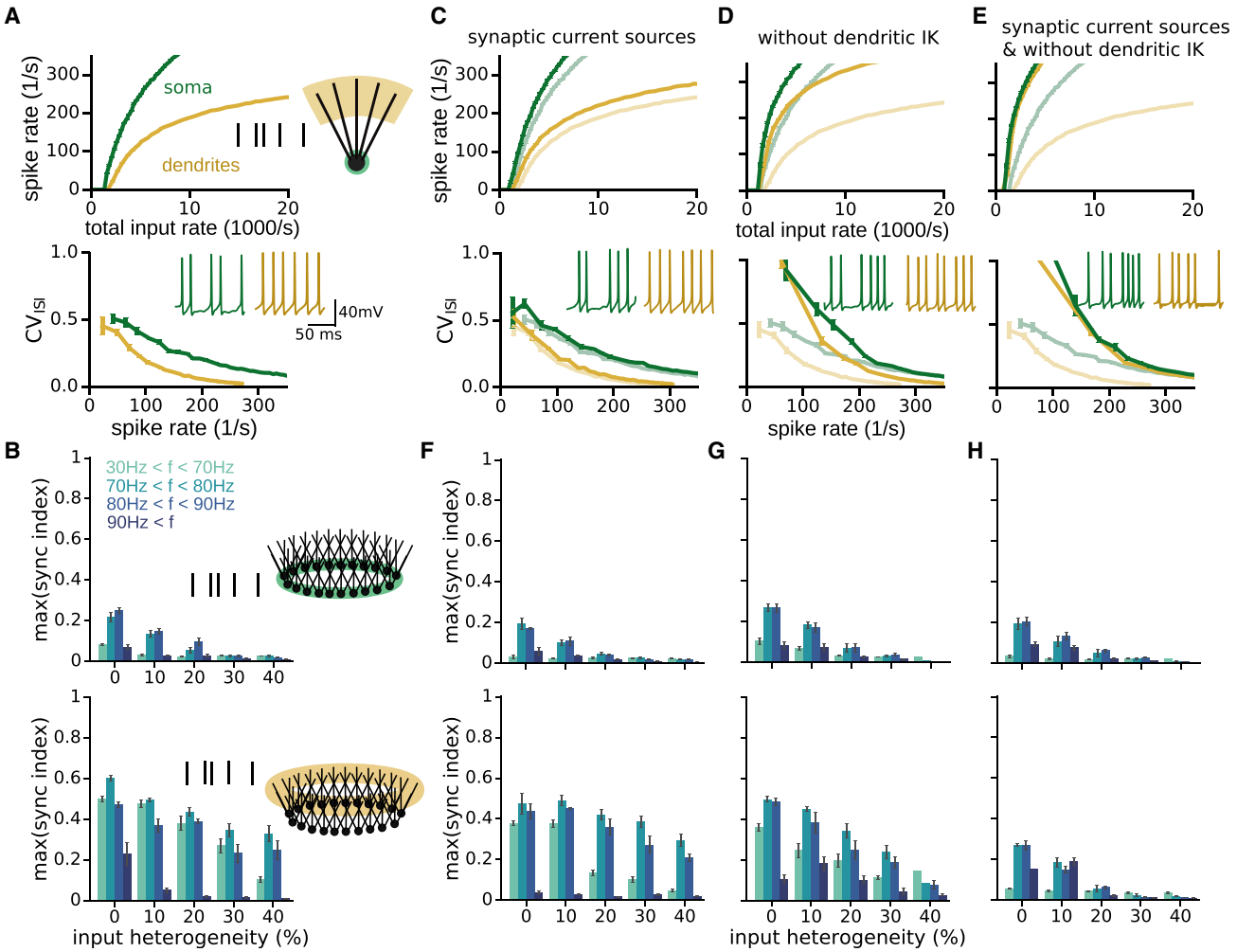

Figure 4. Biophysical mechanisms of PV basket cell dendrites that underlie robust gamma oscillations

(A) Top, I-O relationships of a simplified PV basket cell model (cartoon), driven by excitatory input on the soma (green, 50 synapses) or dendrites (orange, 100 synapses $\geq$ 150 μm from the soma). Bottom, CV of the ISIs as a function of output spike rate. Insets, example spike trains. Mean ± SEM, 10 simulations.

(B) Data from ring networks using 200 simplified PV basket cell models, driven by either soma or dendritic input. Histograms show maximum synchrony index per frequency band, as a function of input heterogeneity. Color code indicates the oscillation frequency bands. Mean ± SEM, 5 network instantiations.

(C) As in (A) but using synaptic current sources instead of synaptic conductances (these synapses have the same kinetics but with a fixed driving force). Faint lines are the data from (A) for comparison.

(D) As in (A) but without dendritic voltage-dependent K^+ channels.

(E) As in (A) but using synaptic current sources and without dendritic K^+ channels.

(F–H) The maximum synchrony index per frequency band, as a function of input heterogeneity, based on ring networks built from PV basket cell models described in (C)–(E). The three different conditions can be compared with the control histograms in (B).

important determinants of network synchron, and that dendrite-driven synchrony is more robust to both for a wide range of parameters.

So far, we used the most elementary network models that produce gamma synchrony. To investigate whether our results depend on specific neuronal or network properties, we performed additional simulations. First, we explored the impact of adding gap junctions to the model (Hormuzdi et al., 2001) (Figures S4A–S4F). We positioned these electrical synapses either near the PV basket cell somata or on the distal dendrites. Regardless of their position, electrical synapses between PV basket cells increase the synchrony index for both dendrite- and soma-driven networks. However, including electrical synapses did not change the conclusion that dendrite-driven synchrony is more robust (Figures S4C and S4F). Second, adding N-methyl-D-aspartate (NMDA) receptors (Koh et al., 1995; Sambandan et al., 2010) enhances the I-O gain for both somatic and dendritic inputs (Figures S5A–S5C) but also did not change our conclusion (Figure S5C). Third, because inhibition can be hyperpolarizing or shunting (Vida et al., 2006), we performed network simulations while varying the reversal potential of inhibition. However, this did also not affect the outcome (Figures S5D–S5F). Fourth, when we changed the network from a one-dimensional (1D) "ring structure" to a 2D network with local

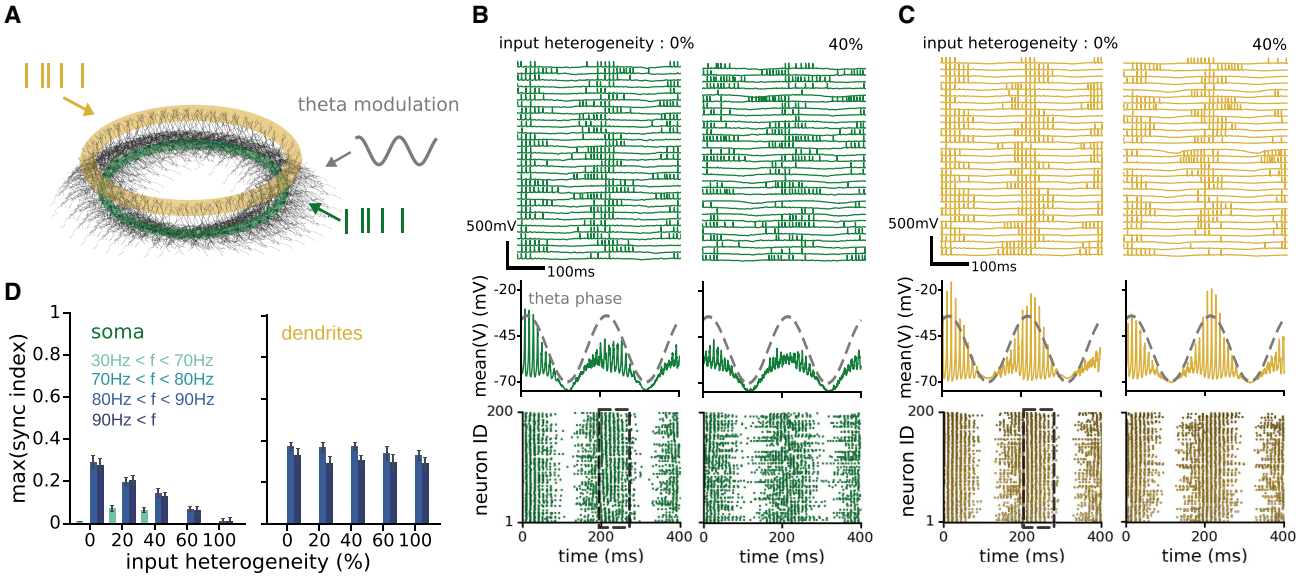

Figure 5. PV basket cell dendrites enhance the robustness of theta-nested gamma rhythms

(A) Ring network of 200 PV basket cell models with a reconstructed morphology. PV basket cells receive a theta frequency-modulated input current to the soma. In addition, networks receive rate-coded excitatory input either close to the soma (green, 50 synapses $\leq$ 50 μm from the soma) or to the dendrites (orange, 100 synapses $\geq$120 μm from soma).

(B) PV basket cell activity in a network driven by perisomatic excitation. Input heterogeneity increases from left to right. Top row, example membrane potential traces showing spikes from 30 random cells. Middle row, mean membrane potential. Dashed line is the theta phase. Bottom row, raster plots of all 200 PV basket cells in the network. Black box, phase interval during which the synchrony index was calculated.

(C) As in (B), but networks are driven with dendritic excitation.

(D) The maximum synchrony index per frequency band, as a function of input heterogeneity. Mean ± SEM, 5 network instantiations, averaged over ten theta cycles.

connectivity based on recent empirical data (Espinoza et al., 2018), dendrite-driven gamma synchrony was also more robust (Figures S6A–S6C). Finally, we constructed composite networks by using a mixture of all five reconstructed PV basket cell models. Because the models have a substantially different excitability (input resistance varies between 57 and 119 MΩ) and morphology (Figure S1A), this cell-to-cell variability adds further spatial heterogeneity and increases the realism of the network. Nevertheless, dendrite-driven gamma synchrony remained more robust (Figures S6D–S6F).

In summary, using anatomically and biophysically detailed network models, we found that input arriving on the dendrites strengthens the robustness of gamma synchrony in heterogeneous networks, and we show that this conclusion holds for a wide range of neuronal and network parameters.

How do PV basket cell dendrites enhance gamma oscillations?

This question is difficult to address in anatomically and biophysically detailed PV basket models because manipulating the dendritic properties also affects the fast-spiking phenotype (Hu et al., 2010). Therefore, we constructed a simpler model to determine the underlying biophysical mechanisms. We used a single somatic compartment and five apical dendrites with similar length and diameter as real PV basket cells (Figure 4A). For the spiking mechanism, we used a well-known model that recapitulates the spiking properties of these cells (Wang-Buzsaki model [Wang and Buzsáki, 1996]; see STAR Methods), and we added the high-threshold-activated K^+ conductance to the dendrites (Hu et al., 2010). The model resembled the measured I-O properties (Figure S7A) and reproduced the synchrony index of the anatomically detailed models (Figures 4A, 4B, and S7B–S7E).

We explored two hypotheses to explain the robustness of dendrite-driven synchrony. First, thin PV basket cell dendrites have a high impedance and strongly depolarize when excited by synaptic inputs. Such strong dendritic depolarizations reduce the magnitude of EPSPs by reducing their driving force, and this will reduce the I-O gain (Bush and Sejnowski, 1994). Furthermore, a reduced driving force will also reduce the amplitude of the membrane-potential fluctuations and enhance spike regularity. To test this hypothesis, we converted excitatory synaptic conductances to currents (which are independent of driving force). Synaptic currents indeed increased the gain of the I-O relationship (Figure 4C) but did not significantly affect spike regularity (quantified by the CV), and the synchrony index was only slightly reduced (compare Figures 4F and 4B). Therefore, this mechanism appears to play only a minor role in enhancing network synchrony, and other mechanisms must exist.

A second hypothesis is that the K^+ conductances in the dendrites reduce the gain of the dendritic I-O relationship by actively opposing dendritic depolarization (Hu et al., 2010). Deleting the K^+ conductance from the dendrites indeed increased the gain (Figure 4D), and interspike intervals became more irregular

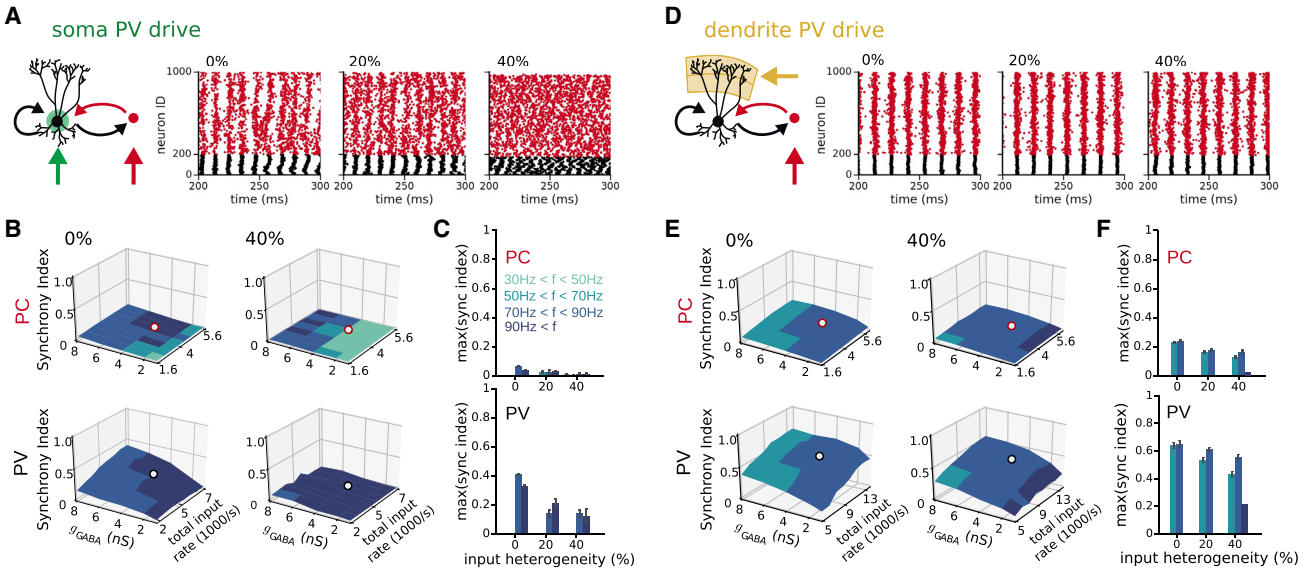

Figure 6. PV basket cell dendrites enhance synchrony in networks of synaptically coupled excitatory and inhibitory neurons

(A) Simulations using networks of reciprocally coupled PV basket cells and principal cells (PCs; see STAR Methods). The PV basket cells are also coupled among themselves. Both populations of cells are driven by an excitatory drive with varying mean rate and input heterogeneity (green and red arrows). The external drive to PV basket cells is located perisomatically (green shaded area). Spike raster diagrams show activity of 200 PV basket cells (black) and 800 PCs (red) for 0%, 20%, and 40% input heterogeneity.

(B) The synchrony index as a function of inhibitory coupling strength (between PV basket cells) and total input rate to PV basket cells for 0% and 40% input heterogeneity (top row: PCs; bottom row: PV basket cells). The dots on the synchrony index correspond to the examples in (A).

(C) The maximum synchrony index per frequency band, as a function of input heterogeneity (PCs, top; PV cells, bottom). Mean ± SEM, 5 network instantiations.

(D–F) Same as (A)–(C) but now using dendritic input to PV basket cells (yellow shaded area).

(Figure 4D). Furthermore, dendrite-driven synchrony became slightly more sensitive to input heterogeneity (Figure 4G). However, the difference between soma- and dendrite-driven synchrony was still striking, indicating that the K^+ conductance alone does not explain why dendrite-driven synchrony is more robust (Figure 4G).

Finally, we considered the following hypothesis: the depolarization caused by deleting the voltage-dependent K^+ conductances—which should steeply increase the gain—may be limited because it is compensated by a strong reduction in driving force for synaptic excitation. To test this, we deleted the K^+ conductance from the dendrites and used excitatory synaptic currents instead of conductances to drive spiking in PV basket cells. In this condition, the gain of both the soma- and dendrite-driven I-O relationship sharply increased (Figure 4E). Furthermore, interspike intervals became very irregular (Figure 4E). In agreement with our hypothesis, dendrite-driven networks were now equally sensitive to input heterogeneity as the soma-driven networks (Figure 4H). Altogether, these data show that dendritic K^+ currents, and to a lesser degree, the reduced driving force for excitation, decrease the I-O gain (enhancing robustness to input heterogeneity) and reduce membrane-potential fluctuations (enhancing robustness to temporal heterogeneity).

PV basket cell dendrites enhance the robustness of theta-nested gamma rhythms

Gamma oscillations often occur superimposed on the slower theta (5–12 Hz) oscillations (Bragin et al., 1995; Pernía-Andrade and Jonas, 2014). Such cross-frequency coupling may serve to couple remote cortical circuits (Colgin, 2015). Therefore, we tested whether dendrites also enhance gamma synchrony when modulated by the theta rhythm. We used the anatomically detailed network models and simulated the theta rhythm by a sinusoidal current (Figure 5A; see STAR Methods). We then compared the robustness of gamma synchrony when driving the network with somatic or dendritic input.

Similar to observations in the dentate gyrus of exploring rats (Bragin et al., 1995), the simulated gamma frequency was in the range of 80–100 Hz. For homogeneous networks (0% heterogeneity), both soma- and dendrite-driven synchrony emerged within a single theta cycle (Figures 5B and 5C). Furthermore, dendrite-driven synchrony was substantially higher compared with soma-driven synchrony (Figures 5B and 5C). With increasing input heterogeneity, soma-driven network synchrony fell rapidly, while dendritic-driven synchrony remained intact for all frequency bands (Figure 5D). These data show that dendrite-driven gamma synchrony superimposed on theta oscillations is also more robust to network heterogeneities.

PV basket cell dendrites enhance synchrony in networks of synaptically coupled excitatory and inhibitory neurons

Models of gamma oscillations in cortical circuits generally fall into two classes: one that generates oscillations with a single pool of inhibitory cells, and one that generates oscillations by the reciprocal connections between pools of inhibitory and

excitatory principal neurons (Tiesinga and Sejnowski, 2009; Whittington et al., 2000). While it is generally thought that the former class captures gamma oscillations in the dentate gyrus (Diamantaki et al., 2016; Espinoza et al., 2018; Ewell and Jones, 2010; Vida et al., 2006), we wanted to test whether our findings also generalize to networks of coupled excitatory and inhibitory neurons.

To test this, we built a model composed of 200 anatomically detailed PV basket cells and 800 principal neurons that were synaptically coupled based on empirical data (Figure 6A, cartoon; see STAR Methods). Both neuronal populations received Poisson-type synaptic stimulation. We considered again two cases that depended on whether PV basket cells were driven by input close to the soma (Figures 6A–6C) or on the dendrites (Figures 6D–6F). In networks with homogeneous input across neurons, synchrony among PV basket cells, and, to a lesser degree, principal neurons emerged rapidly, but as the input heterogeneity increased, synchrony was only maintained when PV basket cells received input on the dendrites (compare Figures 6C and 6F). Lastly, even in homogeneous networks (0% input heterogeneity cases) dendrite-driven networks showed a higher synchrony. This further illustrates, as discussed earlier, that PV basket cell dendrites not only buffer spatial input heterogeneities but also temporal heterogeneities in a variety of network architectures, leading to high neuronal synchrony.

DISCUSSION

We show that PV basket cell dendrites are critically important for enhancing synchronous activity at gamma frequencies in heterogeneous networks. We found that the dendrites scale down the gain of the I-O relationship and reduce the cell's sensitivity to input fluctuations due to the high levels of dendritic K^+ channels. Anatomically detailed network models reveal that these properties help to homogenize firing rates so that PV basket cells can synchronize at a common frequency. Therefore, we propose that the biophysical properties of PV basket cell dendrites enhance the robustness of gamma oscillations.

For decades, experiments and theory have tried to explain how spike synchrony emerges in heterogeneous networks. Classic work studying gamma oscillations *in vitro*, by perfusing brain slices with excitatory receptor agonists (Fisahn et al., 1998; Whittington et al., 1995), showed that fast-spiking cells can synchronize when their input varies between ~35% and ~53% (Vida et al., 2006). However, this likely underestimates the conditions *in vivo* when synaptic input is more cell selective and noisier (Destexhe et al., 2003), favoring desynchronization. Early network models tolerated only 3%–5% heterogeneity of the tonic drive (Wang and Buzsáki, 1996), until reports showed that inhibitory connections between PV basket cells are faster and stronger than previously thought (Bartos et al., 2001, 2002). Based on these data, network models could tolerate a heterogeneous tonic drive up to 10% (Bartos et al., 2002). A landmark study showed that shunting inhibition further enhances robustness and increases tolerance to heterogeneous input of 30%–70% (Vida et al., 2006). However, the enhancing effects of shunting inhibition only work under restrictive conditions as it is dependent on a low excitatory drive and strong inhibitory coupling (Vida et al., 2006). Because of the strong compound shunting inhibition (Figure S2C, bottom panel), the model generates gamma oscillations in the absence of excitatory input, driven by the interaction of shunting inhibition and a persistent Na^+ current, and desynchronizes as excitation increases (Figure S2B). This is unlikely to occur in biological networks; therefore, a key mechanism for synchrony in heterogeneous networks with realistic inhibitory coupling was lacking.

By considering the dendrites, we show that networks can tolerate high levels of input heterogeneity, well beyond 100%. This finding is independent of whether inhibition is hyperpolarizing or shunting and relaxes the requirement for strong inhibitory coupling by an order of magnitude (Figure S2C). We also increased biological realism to the model network by adding other forms of heterogeneity. Previous models mainly used tonic excitation. Instead, we used Poisson trains of synaptic conductances, adding a significant amount of synaptic noise that reduces synchrony (Figure S3D). We also used networks composed of different cell models, each with a unique morphology and excitability, resembling biological networks (Figure S6F). Finally, we show that PV basket cells in highly heterogeneous networks can synchronize during hippocampal theta oscillations (Figure 5) and in different network architectures (Figure 6). In summary, PV basket cell dendrites strongly enhance spike synchrony in inhibitory networks under a wide range of conditions, which is necessary to withstand the plethora of heterogeneities that is typical for biological networks.

What are the biophysical mechanisms that enable PV basket cell dendrites to enhance spike synchrony? We find that two factors play a role. First, PV basket cell dendrites lack regenerative events such as Na^+ and Ca^{2+} spikes (Hu et al., 2010) and have only low levels of NMDA receptors (Koh et al., 1995). Instead, they are dominated by high-threshold and fast-activating K^+ conductances (Hu et al., 2010). Second, thin PV basket cell dendrites have a high input impedance and rapidly depolarize when driven by synaptic inputs. This reduces the driving force for excitation and limits the amount of synaptic current that can be generated (Bush and Sejnowski, 1994). Consequently, the I-O relationship of PV basket cells displays a shallow slope and rapidly saturates in response to dendritic inputs with incremental intensities (Figure 4). Such an I-O relationship compresses the dynamic range of PV basket cell output firing and reduces the sensitivity for detecting changes in input strength. When individual PV basket cells in the network are targeted by excitatory inputs of heterogeneous intensities, this dendritic feature contributes to synchrony by helping to homogenize the firing rate over the basket cell population. Beside the gain, the I-O relationship is also characterized by the rheobase, or the minimal current necessary to evoke spiking. For distributed synaptic input, the rheobase for dendritic input is slightly higher compared with somatic input (Figures 4A and 4C–4E, top panels), but this factor does not play a major role in network synchronization. However, we should note that a higher rheobase and sublinear I-O relationship, typical for dendrite-driven spiking, requires more synaptic input to reach the same spike frequency, which may be metabolically more costly (Attwell and Laughlin, 2001). Among the mechanisms that reduce gain, the dendritic K^+ conductances play a more important role (Figure 4). Yet, surprisingly, K^+ channels

are not necessary. Without K^+ channels, PV basket cell networks remain robust to heterogeneities because of the enhanced contribution of a reduction in driving force (Figure 4G). Altogether, these data illustrate that care should be taken when simplifying inhibitory neurons as point neurons without dendrites in network models (Poirazi and Papoutsi, 2020; Tzilivaki et al., 2019).

The low gain of the dendritic I-O relationship in PV basket cells stands in contrast to pyramidal neuron dendrites that have a steeper dendritic I-O gain compared with the soma (Larkum et al., 2004). However, the properties of PV basket cells in the dentate gyrus may not be exceptional, and there is evidence that PV basket cells in other circuits have similar dendritic properties (reviewed in Hu and Vervaeke, 2017). One exception is a study showing supra-linear dendritic Ca^{2+} responses in hippocampal CA1 PV-expressing neurons (Chiovini et al., 2014). However, Ca^{2+} responses are an indirect measure of dendritic excitability, and Ca^{2+} changes can be supra-linear while synaptic integration in the dendrites is sub-linear (Tran-Van-Minh et al., 2016). Therefore, it remains to be determined whether PV basket cell dendrites in different brain regions have similar properties. Other rhythm-generating inhibitory neurons in the cerebellar cortex, such as stellate and Golgi cells, also have thin, high impedance dendrites lacking regenerative properties, and the sub-linear integration in these cells is dominated by a reduction in synaptic driving force (Abrahamsson et al., 2012; Tran-Van-Minh et al., 2016; Vervaeke et al., 2012). Therefore, we speculate that some inhibitory interneurons have dendrites that are ideally suited for rhythm generation.

Neurons integrate input from different origins that is spatially segregated on their dendrites. A corollary of our results is that input from the entorhinal cortices on the outer two-thirds of the apical dendrites is more likely to generate gamma oscillations compared with the commissural input that targets the proximal dendrites. Spatial segregation of synaptic inputs on the dendrites is common in the brain. For example, PV basket cells in layer 4 of the neocortex receive thalamic inputs close to the soma, while intra-cortical contacts are rather located on the distal dendrites (Bagnall et al., 2011; Freund et al., 1985). Depending on whether the cortical circuit is dominated by sensory or intracortical activity, this may promote network desynchronization and synchronization, respectively. In conclusion, our results suggest that the biophysical properties of PV basket cell dendrites promote spike synchrony in the gamma frequency range and support the many cognitive functions associated with this rhythm.

Limitations of the study

First, our model does not include all cell types of the dentate gyrus such as excitatory mossy cells and inhibitory cells such as axo-axonic cells, somatostatin-expressing HIPP cells, and CCK-expressing HICAP cells (Halasy and Somogyi, 1993). Quantitative data about their intrinsic properties and network connections are limited, and by focusing on PV basket cells, the model is more amenable to analyzing the underlying biophysical mechanisms. Nevertheless, we cannot exclude that some of these omitted cell types also play a role in generating gamma oscillations. Second, PV basket cells in the brain can also be classified as type 1 and type 2 neurons depending on whether they can fire at an arbitrarily low rate (type 1) or they have a threshold frequency below which they cannot sustain firing (type 2) (Hodgkin, 1948; Tikidji-Hamburyan and Canavier, 2020). Previous work and the data presented here show that PV basket cells in the dentate gyrus and area CA1 are type 1 (Ferguson et al., 2013; Tikidji-Hamburyan and Canavier, 2020), while PV basket cells in the neocortex are type 2 (Tateno et al., 2004). So, it remains to be tested whether the mechanisms shown here generalize to multiple types of PV basket cells.

STAR★METHODS

Detailed methods are provided in the online version of this paper and include the following:

- KEY RESOURCES TABLE
- RESOURCE AVAILABILITY
  - Lead contact
  - Materials availability
  - Data and code availability
- EXPERIMENTAL MODEL AND SUBJECT DETAILS
- METHOD DETAILS
  - Dendritic patch-clamp recordings
  - Anatomically detailed PV basket cell model
  - Model fitting
  - Ball-and-sticks model
  - Principal (granule) cell model
  - AMPA- and GABAergic synaptic conductances
  - Co-localized AMPA/NMDA synapses
  - Current-based synapses
  - Electrical synapses
  - Ring networks of PV basket cells
  - Ring networks of ball-and-stick cells
  - Ring networks of PV basket cells and principal cells
  - Two-dimensional PV basket cell network
  - External drive in anatomically detailed PV cell ring networks, ball-and-stick ring networks and 2D-networks
  - External drive of network of PV basket cells and principal cells (PC)
  - Theta-nested gamma oscillations
  - Simulation setup
- QUANTIFICATION AND STATISTICAL ANALYSIS
  - Gain of input-output (I-O) relationships
  - Spike rates
  - The coefficient of variation of interspike intervals (ISI)
  - Oscillation frequency
  - Synchrony Index
  - Statistical analyses

SUPPLEMENTAL INFORMATION

Supplemental information can be found online at https://doi.org/10.1016/j.celrep.2022.110948.

ACKNOWLEDGMENTS

We thank the members of the Vervaeke lab for discussions and comments on the manuscript and Padraig Gleesson for his continuous support of neuroML.

This work was supported by an ERC starting grant (639272) to K.V.; a Young Research Talents grant from the Norwegian Research Council to K.V. (513401); a Toppforsk grant from the Norwegian Research Council (#276047) to H.H. and K.V.; an EEA grant (RO-NO-2019-0504) to K.V., and an EU Seventh Framework Scientia Fellows fellowship to B.K. (609020, FP-PEOPLE-2013-COFUND). H.H. was also supported by the Norwegian Research Council (#250866). We thank Aaron Millstein, Raul Muresan, Christoph Schmidt-Hieber, and Alexandra Tran-Van-Minh for providing critical comments that significantly improved a draft of the manuscript.

AUTHOR CONTRIBUTIONS

B.K. and K.V. designed the study. B.K. performed all simulations and analyses. H.H. performed the patch-clamp experiments. B.K. and K.V. wrote the paper. All authors discussed the results.

DECLARATION OF INTERESTS

The authors declare no competing interests.

Received: August 6, 2021
Revised: February 7, 2022
Accepted: May 21, 2022
Published: June 14, 2022

REFERENCES

Abrahamsson, T., Cathala, L., Matsui, K., Shigemoto, R., and DiGregorio, D.A. (2012). Thin dendrites of cerebellar interneurons confer sublinear synaptic integration and a gradient of short-term plasticity. Neuron *73*, 1159–1172. https://doi.org/10.1016/j.neuron.2012.01.027.

Amaral, D.G., Scharfman, H.E., and Lavenex, P. (2007). The dentate gyrus: fundamental neuroanatomical organization. In Prog. Brain Res., pp. 3–790. https://doi.org/10.1016/s0079-6123(07)63001-5.

Attwell, D., and Laughlin, S.B. (2001). An energy budget for signaling in the grey matter of the brain. J. Cereb. Blood Flow Metab. *21*, 1133–1145. https://doi.org/10.1097/00004647-200110000-00001.

Bagnall, M.W., Hull, C., Bushong, E.A., Ellisman, M.H., and Scanziani, M. (2011). Multiple clusters of release sites formed by individual thalamic afferents onto cortical interneurons ensure reliable transmission. Neuron *71*, 180–194. https://doi.org/10.1016/j.neuron.2011.05.032.

Bartos, M., Vida, I., Frotscher, M., Geiger, J.R.P., and Jonas, P. (2001). Rapid signaling at inhibitory synapses in a dentate gyrus interneuron network. J. Neurosci. *21*, 2687–2698. https://doi.org/10.1523/jneurosci.21-08-02687.2001.

Bartos, M., Vida, I., Frotscher, M., Meyer, A., Monyer, H., Geiger, J.R.P., and Jonas, P. (2002). Fast synaptic inhibition promotes synchronized gamma oscillations in hippocampal interneuron networks. Proc. Natl. Acad. Sci. U S A *99*, 13222–13227. https://doi.org/10.1073/pnas.192233099.

Bartos, M., Vida, I., and Jonas, P. (2007). Synaptic mechanisms of synchronized gamma oscillations in inhibitory interneuron networks. Nat. Rev. Neurosci. *8*, 45–56. https://doi.org/10.1038/nrn2044.

Bragin, A., Jando, G., Nadasdy, Z., Hetke, J., Wise, K., and Buzsaki, G. (1995). Gamma (40-100 Hz) oscillation in the hippocampus of the behaving rat. J. Neurosci. *15*, 47–60. https://doi.org/10.1523/jneurosci.15-01-00047.1995.

Bush, P.C., and Sejnowski, T.J. (1994). Effects of inhibition and dendritic saturation in simulated neocortical pyramidal cells. J. Neurophysiol. *71*, 2183–2193. https://doi.org/10.1152/jn.1994.71.6.2183.

Buzsáki, G., and Wang, X.-J. (2012). Mechanisms of gamma oscillations. Annu. Rev. Neurosci. *35*, 203–225. https://doi.org/10.1146/annurev-neuro-062111-150444.

Calvin, W.H., and Stevens, C.F. (1967). Synaptic noise as a source of variability in the interval between action potentials. Science *155*, 842–844. https://doi.org/10.1126/science.155.3764.842.

Cannon, R.C., Gleeson, P., Crook, S., Ganapathy, G., Marin, B., Piasini, E., and Silver, R.A. (2014). LEMS: a language for expressing complex biological models in concise and hierarchical form and its use in underpinning NeuroML 2. Front. Neuroinform. *8*, 79. https://doi.org/10.3389/fninf.2014.00079.

Cardin, J.A., Carlén, M., Meletis, K., Knoblich, U., Zhang, F., Deisseroth, K., Tsai, L.-H., and Moore, C.I. (2009). Driving fast-spiking cells induces gamma rhythm and controls sensory responses. Nature *459*, 663–667. https://doi.org/10.1038/nature08002.

Carnevale, N.T., and Hines, M.L. (2006). The NEURON Book (Cambridge University Press). https://doi.org/10.1017/cbo9780511541612.005.

Chiovini, B., Turi, G.F., Katona, G., Kaszás, A., Pálfi, D., Maák, P., Szalay, G., Szabó, M.F., Szabó, G., Szadai, Z., et al. (2014). Dendritic spikes induce ripples in parvalbumin interneurons during hippocampal sharp waves. Neuron *82*, 908–924. https://doi.org/10.1016/j.neuron.2014.04.004.

Claiborne, B.J., Amaral, D.G., and Cowan, W.M. (1990). Quantitative, three-dimensional analysis of granule cell dendrites in the rat dentate gyrus. J. Comp. Neurol. *302*, 206–219. https://doi.org/10.1002/cne.903020203.

Colgin, L.L. (2015). Theta–gamma coupling in the entorhinal–hippocampal system. Curr. Opin. Neurobiol. *31*, 45–50. https://doi.org/10.1016/j.conb.2014.08.001.

Cornford, J.H., Mercier, M.S., Leite, M., Magloire, V., Häusser, M., and Kullmann, D.M. (2019). Dendritic NMDA receptors in parvalbumin neurons enable strong and stable neuronal assemblies. Elife *8*, e49872. https://doi.org/10.7554/elife.49872.

Csicsvari, J., Jamieson, B., Wise, K.D., and Buzsáki, G. (2003). Mechanisms of gamma oscillations in the hippocampus of the behaving rat. Neuron *37*, 311–322. https://doi.org/10.1016/s0896-6273(02)01169-8.

Destexhe, A., Rudolph, M., and Paré, D. (2003). The high-conductance state of neocortical neurons in vivo. Nat. Rev. Neurosci. *4*, 739–751. https://doi.org/10.1038/nrn1198.

Diamantaki, M., Frey, M., Berens, P., Preston-Ferrer, P., and Burgalossi, A. (2016). Sparse activity of identified dentate granule cells during spatial exploration. ELife *5*, e20252. https://doi.org/10.7554/elife.20252.

Erisir, A., Lau, D., Rudy, B., and Leonard, C.S. (1999). Function of specific K + channels in sustained high-frequency firing of fast-spiking neocortical interneurons. J. Neurophysiol. *82*, 2476–2489. https://doi.org/10.1152/jn.1999.82.5.2476.

Espinoza, C., Guzman, S.J., Zhang, X., and Jonas, P. (2018). Parvalbumin+ interneurons obey unique connectivity rules and establish a powerful lateral-inhibition microcircuit in dentate gyrus. Nat. Commun. *9*, 4605–4610. https://doi.org/10.1038/s41467-018-06899-3.

Ewell, L.A., and Jones, M.V. (2010). Frequency-tuned distribution of inhibition in the dentate gyrus. J. Neurosci. *30*, 12597–12607. https://doi.org/10.1523/jneurosci.1854-10.2010.

Farinella, M., Ruedt, D.T., Gleeson, P., Lanore, F., and Silver, R.A. (2014). Glutamate-bound NMDARs arising from in vivo-like network activity extend spatio-temporal integration in a L5 cortical pyramidal cell model. PLoS Comput. Biol. *10*, e1003590–21. https://doi.org/10.1371/journal.pcbi.1003590.

Ferguson, K.A., Huh, C.Y.L., Amilhon, B., Williams, S., and Skinner, F.K. (2013). Experimentally constrained CA1 fast-firing parvalbumin-positive interneuron network models exhibit sharp transitions into coherent high frequency rhythms. Front. Comput. Neurosc. *7*, 144. https://doi.org/10.3389/fncom.2013.00144.

Fisahn, A., Pike, F.G., Buhl, E.H., and Paulsen, O. (1998). Cholinergic induction of network oscillations at 40 Hz in the hippocampus in vitro. Nature *394*, 186–189. https://doi.org/10.1038/28179.

Freund, T.F., Martin, K.A.C., and Whitteridge, D. (1985). Innervation of cat visual areas 17 and 18 by physiologically identified X- and Y- type thalamic afferents. I. Arborization patterns and quantitative distribution of postsynaptic elements. J. Comp. Neurol. *242*, 263–274. https://doi.org/10.1002/cne.902420208.

Fries, P., Reynolds, J.H., Rorie, A.E., and Desimone, R. (2001). Modulation of oscillatory neuronal synchronization by selective visual attention. Science *291*, 1560–1563. https://doi.org/10.1126/science.1055465.

Fuchs, E.C., Zivkovic, A.R., Cunningham, M.O., Middleton, S., LeBeau, F.E.N., Bannerman, D.M., Rozov, A., Whittington, M.A., Traub, R.D., Rawlins, J.N.P., and Monyer, H. (2007). Recruitment of parvalbumin-positive interneurons determines hippocampal function and associated behavior. Neuron *53*, 591–604. https://doi.org/10.1016/j.neuron.2007.01.031.

Geiger, J.R., Lübke, J., Roth, A., Frotscher, M., and Jonas, P. (1997). Submillisecond AMPA receptor-mediated signaling at a principal neuron-interneuron synapse. Neuron *18*, 1009–1023. https://doi.org/10.1016/s0896-6273(00)80339-6.

Goldberg, E.M., Clark, B.D., Zagha, E., Nahmani, M., Erisir, A., and Rudy, B. (2008). K+ channels at the axon initial segment dampen near-threshold excitability of neocortical fast-spiking GABAergic interneurons. Neuron *58*, 387–400. https://doi.org/10.1016/j.neuron.2008.03.003.

Gray, C.M., König, P., Engel, A.K., and Singer, W. (1989). Oscillatory responses in cat visual cortex exhibit inter-columnar synchronization which reflects global stimulus properties. Nature *338*, 334–337. https://doi.org/10.1038/338334a0.

Halasy, K., and Somogyi, P. (1993). Subdivisions in the multiple GABAergic innervation of granule cells in the dentate gyrus of the rat Hippocampus. Eur. J. Neurosci. *5*, 411–429. https://doi.org/10.1111/j.1460-9568.1993.tb00508.x.

Hodgkin, A.L. (1948). The local electric changes associated with repetitive action in a non-medullated axon. J. Physiol. *107*, 165–181. https://doi.org/10.1113/jphysiol.1948.sp004260.

Hormuzdi, S.G., Pais, I., LeBeau, F.E., Towers, S.K., Rozov, A., Buhl, E.H., Whittington, M.A., and Monyer, H. (2001). Impaired electrical signaling disrupts gamma frequency oscillations in connexin 36-deficient mice. Neuron *31*, 487–495. https://doi.org/10.1016/s0896-6273(01)00387-7.

Hu, H., and Jonas, P. (2014). A supercritical density of Na(+) channels ensures fast signaling in GABAergic interneuron axons. Nat. Neurosci. *17*, 686–693. https://doi.org/10.1038/nn.3678.

Hu, H., and Vervaeke, K. (2017). Synaptic integration in cortical inhibitory neuron dendrites. Neuroscience *368*, 115–131. https://doi.org/10.1016/j.neuroscience.2017.06.065.

Hu, H., Martina, M., and Jonas, P. (2010). Dendritic mechanisms underlying rapid synaptic activation of fast-spiking hippocampal interneurons. Science *327*, 52–58. https://doi.org/10.1126/science.1177876.

Hu, H., Gan, J., and Jonas, P. (2014). Fast-spiking, parvalbumin+ GABAergic interneurons: from cellular design to microcircuit function. Science *345*, 1255263. https://doi.org/10.1126/science.1255263.

Kleppe, I.C., and Robinson, H.P.C. (1999). Determining the activation time course of synaptic AMPA receptors from openings of colocalized NMDA receptors. Biophys. J. *77*, 1418–1427. https://doi.org/10.1016/s0006-3495(99)76990-0.

Koh, D.S., Geiger, J.R., Jonas, P., and Sakmann, B. (1995). Ca(2+)-permeable AMPA and NMDA receptor channels in basket cells of rat hippocampal dentate gyrus. J. Physiol. *485*, 383–402. https://doi.org/10.1113/jphysiol.1995.sp020737.

Kopell, N., and Ermentrout, B. (2004). Chemical and electrical synapses perform complementary roles in the synchronization of interneuronal networks. Proc. Natl. Acad. Sci. U S A *101*, 15482–15487. https://doi.org/10.1073/pnas.0406343101.

Larkum, M.E., Senn, W., and Lüscher, H.-R. (2004). Top-down dendritic input increases the gain of layer 5 pyramidal neurons. Cereb. Cortex *14*, 1059–1070. https://doi.org/10.1093/cercor/bhh065.

Lisman, J.E., and Idiart, M.A.P. (1995). Storage of 7 ± 2 short-term memories in oscillatory subcycles. Science *267*, 1512–1515. https://doi.org/10.1126/science.7878473.

Lundqvist, M., Rose, J., Herman, P., Brincat, S.L., Buschman, T.J., and Miller, E.K. (2016). Gamma and beta bursts underlie working memory. Neuron *90*, 152–164. https://doi.org/10.1016/j.neuron.2016.02.028.

Moca, V.V., Nikolić, D., Singer, W., and Mureşan, R.C. (2012). Membrane resonance enables stable and robust gamma oscillations. Cereb. Cortex *24*, 119–142. https://doi.org/10.1093/cercor/bhs293.

Neltner, L., Hansel, D., Mato, G., and Meunier, C. (2000). Synchrony in heterogeneous networks of spiking neurons. Neural Comput. *12*, 1607–1641. https://doi.org/10.1162/089976600300015286.

Nörenberg, A., Hu, H., Vida, I., Bartos, M., and Jonas, P. (2010). Distinct nonuniform cable properties optimize rapid and efficient activation of fast-spiking GABAergic interneurons. Proc. Natl. Acad. Sci. U S A *107*, 894–899. https://doi.org/10.1073/pnas.0910716107.

Pernía-Andrade, A.J., and Jonas, P. (2014). Theta-gamma-modulated synaptic currents in hippocampal granule cells in vivo define a mechanism for network oscillations. Neuron *81*, 140–152. https://doi.org/10.1016/j.neuron.2013.09.046.

Pike, F.G., Goddard, R.S., Suckling, J.M., Ganter, P., Kasthuri, N., and Paulsen, O. (2000). Distinct frequency preferences of different types of rat hippocampal neurones in response to oscillatory input currents. J. Physiol. *529*, 205–213. https://doi.org/10.1111/j.1469-7793.2000.00205.x.

Poirazi, P., and Papoutsi, A. (2020). Illuminating dendritic function with computational models. Nat. Rev. Neurosci. *21*, 303–321. https://doi.org/10.1038/s41583-020-0301-7.

Sambandan, S., Sauer, J.-F., Vida, I., and Bartos, M. (2010). Associative plasticity at excitatory synapses facilitates recruitment of fast-spiking interneurons in the dentate gyrus. J. Neurosci. *30*, 11826–11837. https://doi.org/10.1523/jneurosci.2012-10.2010.

Sik, A., Penttonen, M., Ylinen, A., and Buzsáki, G. (1995). Hippocampal CA1 interneurons: an in vivo intracellular labeling study. J. Neurosci. *15*, 6651–6665. https://doi.org/10.1523/jneurosci.15-10-06651.1995.

Silver, R.A. (2010). Neuronal arithmetic. Nat. Rev. Neurosci. *11*, 474–489. https://doi.org/10.1038/nrn2864.

Softky, W., and Koch, C. (1993). The highly irregular firing of cortical cells is inconsistent with temporal integration of random EPSPs. J. Neurosci. *13*, 334–350. https://doi.org/10.1523/jneurosci.13-01-00334.1993.

Sohal, V.S., Zhang, F., Yizhar, O., and Deisseroth, K. (2009). Parvalbumin neurons and gamma rhythms enhance cortical circuit performance. Nature *459*, 698–702. https://doi.org/10.1038/nature07991.

Strüber, M., Jonas, P., and Bartos, M. (2015). Strength and duration of perisomatic GABAergic inhibition depend on distance between synaptically connected cells. Proc. Natl. Acad. Sci. U S A *112*, 1220–1225. https://doi.org/10.1073/pnas.1412996112.

Strüber, M., Sauer, J.-F., Jonas, P., and Bartos, M. (2017). Distance-dependent inhibition facilitates focality of gamma oscillations in the dentate gyrus. Nat. Commun. *8*, 758–815. https://doi.org/10.1038/s41467-017-00936-3.

Tateno, T., Harsch, A., and Robinson, H.P.C. (2004). Threshold firing frequency–current relationships of neurons in rat somatosensory cortex: type 1 and type 2 dynamics. J. Neurophysiol. *92*, 2283–2294. https://doi.org/10.1152/jn.00109.2004.

Tiesinga, P., and Sejnowski, T.J. (2009). Cortical enlightenment: are attentional gamma oscillations driven by ING or PING? Neuron *63*, 727–732. https://doi.org/10.1016/j.neuron.2009.09.009.

Tiesinga, P.H.E., and José, J.V. (2000). Robust gamma oscillations in networks of inhibitory hippocampal interneurons. Netw. Comput. Neural Syst. *11*, 1–23. https://doi.org/10.1088/0954-898x_11_1_301.

Tikidji-Hamburyan, R.A., and Canavier, C.C. (2020). Shunting inhibition improves synchronization in heterogeneous inhibitory interneuronal networks with type 1 excitability whereas hyperpolarizing inhibition is better for type 2 excitability. Eneuro *7*, ENEURO.0464. https://doi.org/10.1523/eneuro.0464-19.2020.

Tikidji-Hamburyan, R.A., Martínez, J.J., White, J.A., and Canavier, C.C. (2015). Resonant interneurons can increase robustness of gamma oscillations.

J. Neurosci. *35*, 15682–15695. https://doi.org/10.1523/jneurosci.2601-15.2015.

Tort, A.B.L., Rotstein, H.G., Dugladze, T., Gloveli, T., and Kopell, N.J. (2007). On the formation of gamma-coherent cell assemblies by oriens lacunosum-moleculare interneurons in the hippocampus. Proc. Natl. Acad. Sci. U S A *104*, 13490–13495. https://doi.org/10.1073/pnas.0705708104.

Towers, S.K., LeBeau, F.E.N., Gloveli, T., Traub, R.D., Whittington, M.A., and Buhl, E.H. (2002). Fast network oscillations in the rat dentate gyrus in vitro. J. Neurophysiol. *87*, 1165–1168. https://doi.org/10.1152/jn.00495.2001.

Tran-Van-Minh, A., Abrahamsson, T., Cathala, L., and DiGregorio, D.A. (2016). Differential dendritic integration of synaptic potentials and calcium in cerebellar interneurons. Neuron *91*, 837–850. https://doi.org/10.1016/j.neuron.2016.07.029.

Tzilivaki, A., Kastellakis, G., and Poirazi, P. (2019). Challenging the point neuron dogma: FS basket cells as 2-stage nonlinear integrators. Nat. Commun. *10*, 3664. https://doi.org/10.1038/s41467-019-11537-7.

Vella, M., Cannon, R.C., Crook, S., Davison, A.P., Ganapathy, G., Robinson, H.P.C., Silver, R.A., and Gleeson, P. (2014). libNeuroML and PyLEMS: using Python to combine procedural and declarative modeling approaches in computational neuroscience. Front. Neuroinform. *8*, 38. https://doi.org/10.3389/fninf.2014.00038.

Venance, L., Rozov, A., Blatow, M., Burnashev, N., Feldmeyer, D., and Monyer, H. (2000). Connexin expression in electrically coupled postnatal rat brain neurons. Proc. Natl. Acad. Sci. U S A *97*, 10260–10265. https://doi.org/10.1073/pnas.160037097.

Vervaeke, K., Lorincz, A., Nusser, Z., and Silver, R.A. (2012). Gap junctions compensate for sublinear dendritic integration in an inhibitory network. Science *335*, 1624–1628. https://doi.org/10.1126/science.1215101.

Vida, I., Bartos, M., and Jonas, P. (2006). Shunting inhibition improves robustness of gamma oscillations in hippocampal interneuron networks by homogenizing firing rates. Neuron *49*, 107–117. https://doi.org/10.1016/j.neuron.2005.11.036.

Wang, X.-J. (2010). Neurophysiological and computational principles of cortical rhythms in cognition. Physiol. Rev. *90*, 1195–1268. https://doi.org/10.1152/physrev.00035.2008.

Wang, X.-J., and Buzsáki, G. (1996). Gamma oscillation by synaptic inhibition in a hippocampal interneuronal network model. J. Neurosci. *16*, 6402–6413. https://doi.org/10.1523/jneurosci.16-20-06402.1996.

White, J.A., Chow, C.C., Rit, J., Soto-Treviño, C., and Kopell, N. (1998). Synchronization and oscillatory dynamics in heterogeneous, mutually inhibited neurons. J. Comput. Neurosci. *5*, 5–16. https://doi.org/10.1023/a:1008841325921.

Whittington, M.A., Traub, R.D., and Jefferys, J.G.R. (1995). Synchronized oscillations in interneuron networks driven by metabotropic glutamate receptor activation. Nature *373*, 612–615. https://doi.org/10.1038/373612a0.

Whittington, M.A., Traub, R.D., Kopell, N., Ermentrout, B., and Buhl, E.H. (2000). Inhibition-based rhythms: experimental and mathematical observations on network dynamics. Int. J. Psychophysiol. *38*, 315–336. https://doi.org/10.1016/s0167-8760(00)00173-2.

STAR★METHODS

KEY RESOURCES TABLE

REAGENT or RESOURCE	SOURCE	IDENTIFIER
Chemicals, peptides, and recombinant proteins		
SR95531	Tocris	1262
DL-APV	Tocirs	0105
Alexa Fluor 488 hydrazide	Thermo Fisher Scientific	A10436
$CaCl_2$	VWR	22317.297
D-glucose	VWR	101175P
DL-AP5	Tocris	0105
EGTA	Sigma-Aldrich	E4378
HEPES	Sigma-Aldrich	H3375
K-gluconate	Sigma-Aldrich	G4500
KCl	VWR	26764.298
$MgCl_2$	VWR	25108.260
Na_2ATP	Sigma-Aldrich	A2383
NaCl	VWR	27810.364
NaH_2PO_4	VWR	28013.264
$NaHCO_3$	VWR	27778.293
Sucrose	VWR	27480.294
Tetrodotoxin	Alomone labs	T-550
ZD7288	Tocris	1000
Experimental models: Organisms/strains		
Wistar rats	Charles River	Strain code: 273
Software and algorithms		
pClamp	Molecular devices	V9.2.1.9 and 10.3.1.4
Dentate gyrus basket cell model morphologies	Nörenberg A, Hu H, Vida I, Bartos M, Jonas P (2010) PNAS 107:894-9	https://senselab.med.yale.edu/ModelDB/ShowModel?model=140789#tabs-2
Dentate gyrus granule GLU cell model	Strüber M, Sauer J-F, Jonas P and Bartos M (2017) Nature Communications 8:758	https://senselab.med.yale.edu/ModelDB/showmodel?model=229750#tabs-2
Single compartment model of PV cells with shunting inhibition	Vida I, Bartos M, and Jonas P (2006) Neuron 49:107-117	https://senselab.med.yale.edu/ModelDB/ShowModel?model=21329#tabs-2
NEURON Release 7.4	Carnevale, N.T. and Hines, M.L. The NEURON Book Cambridge, UK: Cambridge University Press, 2006.	https://neuron.yale.edu/neuron/download
NeuroML2 Version 0.2.39	Cannon RC, Gleeson P, Crook S, Ganapathy G, Marin B, Piasini E and Silver RA (2014) Frontiers in Neuroinformatics 8: 79.	https://github.com/NeuroML/NeuroML2
PyNeuroML Version 0.3.11 (jNeuroML-0.10.1; libNeuroML-0.2.39;PyLEMS-0.4.9.1)	Vella M, Cannon RC, Crook S, Davison AP, Ganapathy G, Robinson HP, Silver RA and Gleeson P (2014) Frontiers in Neuroinformatics 8: 38.	https://github.com/NeuroML/pyNeuroML
Python/2.7.15	https://www.python.org	https://www.python.org/downloads/
NumPy/1.14.1	https://numpy.org/	https://github.com/numpy
SciPy/0.19.0	https://scipy.org/	https://github.com/scipy
Matplotlib/1.5.1	https://matplotlib.org/	https://github.com/matplotlib/matplotlib
Basic simulation scripts	This paper	https://doi.org/10.5281/zenodo.6501138
Volocity	PerkinElmer	V5.5.1
CorelDRAW	Corel Corporation	X8
ImageJ	https://imagej.nih.gov/ij/	V1.51j8

RESOURCE AVAILABILITY

Lead contact

Further information and requests for resources and reagents should be directed to and will be fulfilled by the lead contact, Koen Vervaeke (koenv@medisin.uio.no).

Materials availability

This study did not generate new unique reagents.

Data and code availability

- Dendritic patch-clamp data and simulated data reported in this paper will be shared by the lead contact upon request.
- All original code has been deposited on GitHub and is publicly available as of publication (DOI available in the Key resources table).
- Any additional information required to reanalyze the data reported in this paper is available from the lead contact upon request.

EXPERIMENTAL MODEL AND SUBJECT DETAILS

Data include recordings from 17- to 23-day-old male Wistar rats. Rats were housed under a 12 h light cycle (7 am-7 pm) and dark cycle (7 pm-7 am) and were kept in a litter of 8–10 animals together with the mother in a single cage. All procedures were ethically approved by the Norwegian Food Safety Authority (projects #FOTS 6590, 7480, 19129, 27620). Experiments were performed in accordance with the Norwegian Animal Welfare Act.

METHOD DETAILS

Dendritic patch-clamp recordings

Transverse hippocampal slices (thickness 350 μm) were cut in ice-cold, sucrose-containing physiological extracellular solution using a vibratome (VT1200, Leica Microsystems), incubated in a storage chamber filled with standard physiological extracellular solution at ∼ 34°C for 30 min, and subsequently stored at room temperature (Hu et al., 2010). Standard extracellular solution contained: 125 mM NaCl, 25 mM $NaHCO_3$, 2.5 mM KCl, 1.25 mM NaH_2PO_4, 2 mM $CaCl_2$, 1 mM $MgCl_2$, and 25 mM D-glucose (equilibrated with 95% O_2 and 5% CO_2 gas mixture. Slices were then transferred into a recording chamber and perfused with standard physiological extracellular solution. Current-clamp recordings were performed at near-physiological temperature (∼ 33°C; range: 31–34°C).

For interneuron dendrite recordings, we used the following strategy. First, a somatic recording was obtained using an internal solution containing Alexa Fluor 488 (50 or 100 μM, Invitrogen). Next, after ∼ 30 min of somatic whole-cell recording, the fluorescently labeled axon and dendrites were traced from the parvalbumin expressing (PV) basket cell soma with a Nipkow spinning disk confocal microscope (Volocity, 5.5.1 PerkinElmer, equipped with an Orca camera, Hamamatsu and a solid-state laser with excitation wavelength of 488 nm). Total exposure time was minimized to avoid photodamage. Finally, fluorescent and infrared differential interference contrast (IR-DIC) images were compared, and dendrites were patched under IR-DIC.

Patch pipettes were fabricated from thick-walled borosilicate glass capillaries (outer diameter: 2 mm, inner diameter: 1 mm) with a horizontal pipette puller (P-97, Sutter Instruments). The intracellular solution for soma-dendritic whole-cell recordings contained 120 mM K-gluconate, 20 mM KCl, 10 mM EGTA, 2 mM $MgCl_2$, 2 mM Na_2ATP and 10 mM HEPES, pH adjusted to 7.3 with KOH. The pipette resistance was 2–10 MΩ for somatic recordings and 6–40 MΩ for dendritic recordings. Current-clamp recordings were performed using a Multiclamp 700B amplifier (Molecular Devices). Series resistance was 12–90 MΩ. Somatic recordings with a resting membrane potential of more positive than −50 mV were discarded. Pipette capacitance and series resistance compensation (bridge balance) were applied throughout the experiments. The input-output relationship was determined by injecting 1-s depolarizing current pulses of various amplitudes into the soma at the resting membrane potential (−60.7 ± 0.8 mV).

Signals were sampled at 50 or 100 kHz with a Digidata 1322 converter board (Molecular Devices) and low pass filtered at 10 kHz. Data acquisition and generation of pulse protocols were performed with pClamp 9 or 10 (Molecular Devices).

PV basket cell identification was based on the non-accommodating, fast-spiking phenotype (steady-state spike frequency >150 Hz at physiological temperature in response to 1 s, 0.3- to 1-nA somatic current pulses) and the morphological properties of the axonal arbor, which is largely restricted to the granule cell layer and established basket-like structures around granule cell somata that were visible in the confocal images. In a previous publication (Hu et al., 2010) a large sample of fast-spiking interneurons in the dentate gyrus was analyzed in detail by light microscopy. It was concluded that the fast-spiking phenotype was tightly correlated with the expression of parvalbumin (Hu et al., 2010). Furthermore, 78 of 83 cells were identified as classical basket cells with tangential axon collaterals and basket-like branches around granule cell somata. In contrast, only 5 out of 83 were axo-axonic cells with radial axon collaterals (Hu et al., 2010). Based on these results, the recorded cells were termed PV basket cells throughout this study.

To determine the propagation of EPSPs from the dendrites to the soma (Figure 2A), miniature EPSPs were evoked by ejecting a high osmotic external solution close to the dendritic recording site during simultaneous soma–dendrite recordings with a third patch pipette. 30 μM ZD7288 and 2 μM SR95531 were added to the standard physiological solution in these experiments to block HCN channels and $GABA_A$ receptors. The high osmotic external solution contained 125 mM NaCl, 25 mM $NaHCO_3$, 2.5 mM KCl, 1.25 mM NaH_2PO_4, 2 mM $CaCl_2$, 1 mM $MgCl_2$, 25 mM D-glucose, 300 mM sucrose, 50 μM DL-APV, 30 μM ZD7288, 2 μM SR95531 and 1 μM tetrodotoxin.

Anatomically detailed PV basket cell model

A previous study (Nörenberg et al., 2010) meticulously constrained the passive parameters of the five PV basket cell models based on experimental data (Figure S1). These models can be downloaded from the ModelDB repository (See Key resources table). We summarize the membrane capacitance C_m, axial resistance R_i, leak reversal potential E_{leak} and membrane conductances g_{leak} for each model in Figures S8A and S8B. The leak conductance g_{leak} is spatially inhomogeneous along the dendrites (higher for closer distance d to the soma, lower more distally), as this fits the passive response properties of dentate gyrus PV cells best (Nörenberg et al., 2010). This is defined as:

$$g_{leak}(d) = \begin{cases} g_{leak,prox} & \text{if } d < 120\ \mu m \\ g_{leak,dist} & \text{otherwise} \end{cases} \quad \text{(Equation 1)}$$

The voltage-dependent currents I_{Na}, I_{K1} and I_{K2} are Hodgkin-Huxley-type models based on the Wang-Buzsaki model (Hu et al., 2010; Wang and Buzsáki, 1996). Here, I_{K1} has the original parameters with kinetic factor $\varphi = 2$, while the steady-state activation curve of I_{K2} is more depolarized to match the inward rectification observed in the distal dendrites (see Figure 1E and see section "Model fitting").

The sodium current I_{Na} has an activation variable m and an inactivation variable h. The dynamics of m is assumed to be fast and substituted by the steady-state value m_∞ (Wang and Buzsáki, 1996) such that:

$$I_{Na} = g_{Na} m_\infty^3 h (V - E_{Na}) \quad \text{(Equation 2)}$$

$$m_\infty = \frac{\alpha_m}{\alpha_m + \beta_m}$$

$$\text{with } \alpha_m(V) = \frac{-0.1(V+35)}{\exp(-0.1(V+35) - 1)},$$

$$\text{and } \beta_m(V) = 4\exp\left(-\frac{V+60}{18}\right),$$

$$\text{and } \frac{dh}{dt} = \varphi_{Na}(\alpha_h(V)(1-h) - \beta_h(V)h)$$

$$\text{with } \alpha_h(V) = 0.07\exp\left(-\frac{V+58}{20}\right)$$

$$\text{and } \beta_h(V) = \frac{1}{\exp(-0.1(V+28)+1)}.$$

The potassium current I_{K1} has only an activation variable n_1, such that:

$$I_{K1} = g_{K1} n_1^4 (V - E_{K1}) \quad \text{(Equation 3)}$$

$$\frac{dn_1}{dt} = \varphi_{K1}\left(\alpha_{n_1}(V)(1-n_1) - \beta_{n_1}(V)n_1\right)$$

$$\text{with} \quad \alpha_{n_1}(V) = \frac{-0.01(V+34)}{\exp(-0.1(V+34)-1)},$$

$$\text{and} \quad \beta_{n_1}(V) = 0.125\exp\left(-\frac{V+44}{80}\right).$$

The potassium current I_{K2} has an activation variable n_2, such that:

$$I_{K2} = g_{K2}n_2^4(V - E_{K2}) \qquad \text{(Equation 4)}$$

$$\frac{dn_2}{dt} = \varphi_{K2}\left(\alpha_{n_2}(V)(1-n_2) - \beta_{n_2}(V)n_2\right)$$

$$\text{with} \quad \alpha_{n_2}(V) = \frac{-0.01(V+20)}{\exp(-0.1(V+20)-1)},$$

$$\text{and} \quad \beta_{n_2}(V) = 0.125\exp\left(-\frac{V+30}{40}\right).$$

For I_{Na}, I_{K1} and I_{K2}, the reversal potential E and parameter φ are shown in Figure S8C, and the maximum conductance g and spatial distribution of the current density is summarized in Figure S8D. The voltage-dependence of the steady-state activation curves and time constants of the variables $x = \{m, h, n_1, n_2\}$ are plotted in Figure S9.

Model fitting

For all five reconstructed basket cell models, we used the passive properties as measured in (Nörenberg et al., 2010) (see Figures S8A and S8B). Next, we systematically varied g_{Na}, g_{K1}, g_{k2} and φ to find good fits to the average I-O relationship that was experimentally measured using somatic current injections (Figure 1C). Next, we conducted simulations to test whether the model matches several other experimental observations, in particular the dendritic I-O relationship (Figure 1D), the steady-state membrane potential responses to dendritic (Figure 1E) and somatic current injections, the spike attenuation along the apical dendrites (not shown), and the attenuation of EPSPs along the dendrites (Figures 2A and 2B). If necessary, we slightly adapted g_{Na} and g_{K1} to obtain a better fit to the experimental data. The resulting channel densities are listed in Figure S8D. Compared to I_{K1}, we shifted the steady-state activation curve of I_{K2} to more depolarized potentials to obtain a better fit to the sublinear membrane potential in response to current injections in the dendrites (Figure 1E). Using only I_{K1} on the entire dendritic tree had no significant effects on any of the main results apart from a worse fit to the dendritic V-I relationship. After introduction of the voltage-dependent channels the input resistance of the models remained relatively similar to the experimental observations described in (Nörenberg et al., 2010) (Figure S8E).

Ball-and-sticks model

This model comprises one soma compartment (diameter = length = 25 μm) and five equal dendritic compartments (diameter = 1 μm, length = 300 μm). Passive properties are C_m = 1 μF/cm^2, $g_{leak,soma}$ = 0.16 mS/cm^2, $g_{leak,dend}$ = 0.08 mS/cm^2, E_{leak} = −75 mV, and R_i = 100 Ωcm. The soma has I_{K1} (g_{K1} = 20 mS/cm^2, E_{K1} = −90 mV, φ_{K1} = 5, see Equation 3) and I_{Na} (g_{Na} = 80 mS/cm^2, E_{Na} = 55 mV, φ_{Na} = 5, see Equation 2). The dendrites have only I_{K1} (g_{K1} = 20 mS/cm^2, E_{K1} = −90 mV, φ_{K1} = 5, see Equation 3). For a comparison to experimental data, see Figure S7A.

Principal (granule) cell model

The regular-spiking principal cell model was adapted unmodified from (Strüber et al., 2017) and can be downloaded from the ModelDB repository (see Key resources table). In short, it comprises one soma compartment (diameter = length = 5.6 μm) with passive parameters C_m = 1.01 μF/cm^2, g_{leak} = 0.1 mS/cm^2, E_{leak} = −75 mV, and R_i = 194 Ωcm. Active properties comprise a voltage-gated Na^+ (g_{Na} = 10 mS/cm^2, E_{Na} = 55 mV), and a delayed-rectifier voltage-gated K^+-conductance (g_K = 15 mS/cm^2, E_K = −90 mV).

AMPA- and GABAergic synaptic conductances

We modeled synaptic AMPA and GABA conductances as two-state kinetic scheme synapses (“Exp2Syn” model in NEURON) i.e.,

$$g_{syn}(t) = \overline{g}_{syn}\frac{e^{-t/\tau_{syn}^{rise}} - e^{-t/\tau_{syn}^{decay}}}{e^{-t_{peak}/\tau_{syn}^{rise}} - e^{-t_{peak}/\tau_{syn}^{decay}}}\Theta[t] \quad \text{(Equation 5)}$$

$$t_{peak} = \log\left(\frac{\tau_{syn}^{decay}}{\tau_{syn}^{rise}}\right)\left(\frac{\tau_{syn}^{rise}\,\tau_{syn}^{decay}}{\tau_{syn}^{decay} - \tau_{syn}^{rise}}\right) \quad \text{(Equation 6)}$$

The AMPA receptors kinetics were based on previous work (Geiger et al., 1997; Kleppe and Robinson, 1999) and our own data shown in Figure 2. The postsynaptic currents are given by $EPSC(V,t) = g_{syn,AMPA}(t)(V - E_{syn,AMPA})$. Parameters for GABA-type and AMPA-type synapses are specified in the section "Ring networks of PV basket cells" and summarized in Figure S12A.

Co-localized AMPA/NMDA synapses

The NMDA-conductance is given by an exponential rise and decay time constant, and is voltage-dependent to model the Mg^{2+}-block (Farinella et al., 2014) as (see also Equation 5):

$$g_{NMDA}(t) = \frac{\overline{g}_{NMDA}}{1 + 0.3e^{-0.08V(t)}}\frac{e^{-t/\tau_{syn,NMDA}^{rise}} - e^{-t/\tau_{syn,NMDA}^{decay}}}{e^{-t_{peak}/\tau_{syn,NMDA}^{rise}} - e^{-t_{peak}/\tau_{syn,NMDA}^{decay}}} \quad \text{(Equation 7)}$$

The ratio between the maximum NMDA and AMPA conductance (0.22) and the voltage dependence of the Mg^{2+}-block (Figures S11A and S11B) was based on measurements from fast spiking basket cells in the dentate gyrus (Koh et al., 1995). The parameters are summarized in Figure S12A.

Current-based synapses

Networks driven by *current-based synapses* (Figures 4C and 4E) had identical synaptic time constants and amplitudes as their conductance-based counterparts, but with a membrane-potential fixed to the leak potential E_{leak} (−75 mV for the anatomically detailed models, and −65 mV for the Ball-and-sticks model, respectively). Therefore, synapses are independent of the driving force, that is, $EPSC(V,t) = g_{syn,AMPA}(t)(E_{leak} - E_{syn,AMPA}) = \text{const} \times g_{syn,AMPA}(t)$.

Electrical synapses

We positioned ten gap junctions (Bartos et al., 2002; Vida et al., 2006) randomly either on the perisomatic area ($\leq$ 50 μm from soma, conductance 0.1 nS) or on the outer apical dendrites ($\geq$ 120 μm from soma, conductance 0.35 nS) and coupled each cell to four out of eight randomly chosen nearest neighbours (four to the left, four to the right). Therefore, gap junctions were only present between cells that were at most 200 μm apart (Espinoza et al., 2018) (see also next section "Ring networks of PV basket cells"). We tested the strength of gap junction coupling by measuring the coupling coefficient between electrically coupled cells which was typically around 7–9% for two connected (but otherwise isolated cells) and between 3 and 12% (depending on the distance between cells) in a gap junction coupled network (Espinoza et al., 2018; Hormuzdi et al., 2001; Venance et al., 2000) (Figures S4A and S4D).

Ring networks of PV basket cells

Ring networks are based on previous models of gamma oscillations (Bartos et al., 2002; Vida et al., 2006) (for an overview of network connection parameters, see Figures S12A and S12B). We arranged $N = 200$ PV basket cells along a ring where the distance between neighboring cells is 50 μm. The probability that two neurons are coupled by inhibitory synapses follows a Gaussian distribution $p_{ring}(d) = e^{-d^2/2\sigma^2}$, with d being the distance between the cell somata, and $\sigma = 1200$ μm (Bartos et al., 2002; Vida et al., 2006) (Figures 3A and S10A). Synaptic connections are not allowed between cells that are more than 2500 μm apart. According to these rules, each PV basket cell is connected to approximately 58 other PV basket cells. These rules are constrained by empirical data of the PV basket cell density and the extent of their axonal tree in hippocampal area CA1 (Sik et al., 1995).

When two cells are synaptically connected, we randomly distributed n synapses in the perisomatic region ($\leq$ 50 μm from soma). The number of synapses between two PV basket cells was distance-dependent following the same equation as the coupling probability, but with a maximum of five synapses. The number of synaptic contacts was rounded down to an integer (Figure S10B).

The synaptic time constants are listed in Figure S12A. We varied the maximum conductance of the GABAergic synapses $\overline{g}_{syn,GABA}$ between 0.5 and 10 nS ($\approx$ 0.008–0.08 mS/cm^2), with a synaptic reversal potential $E_{syn,GABA} = -75$ mV for hyperpolarizing inhibition, and −60 mV for shunting inhibition. For shunting inhibition, we varied $\overline{g}_{syn,GABA}$ up to 30 nS, because synchronous states typically require very strong inhibition (Tikidji-Hamburyan and Canavier, 2020; Vida et al., 2006). Synaptic currents are described by $IPSC(V,t) = g_{syn,GABA}(t)(V - E_{syn,GABA})$.

The spike conductance delay τ comprised a constant synaptic delay of $\tau_0 = 0.5$ ms and a distance-dependent delay of $\tau_i = 0.2i$ ms, where i is the absolute difference between the indices of two neurons on the ring network (Bartos et al., 2002; Vida et al., 2006). Given that neighboring neurons are separated by 50 μm, this corresponds to a conduction velocity of 0.25 m/s). In a network of 200

cells, the conduction delays varied between 0.7 ms and 10.5 ms, with an average delay $\tau \approx 4.1$ ms. To avoid onset transients, the network synapses were only activated after 150 ms into the simulation.

Ring networks of ball-and-stick cells

Ring networks of Ball-and-stick model neurons were the same as those comprising detailed PV basket cell neurons, with the exception that synapses between Ball-and-stick neurons were confined to the somatic compartment.

Ring networks of PV basket cells and principal cells

Networks of coupled excitatory and inhibitory cells consisted of $N_I = 200$ PV basket cells and $N_E = 4N_I$ principal cells (PC), respectively, arranged on two rings. The spatial footprint of PV→PC was the same as for PV→PV, i.e., $p_{\text{ring}}(d) = c\, e^{-d^2/2\sigma^2}$ with $\sigma = 1200$ μm (see Figure S10A). For PV→PV connectivity, $c = 1$, resulting in ∼ 58 connections per cell, while for PV→PC, $c = 0.35$, resulting in ∼ 20 connections from PV cells to any PC (Strüber et al., 2017). The footprint from PC→PV was Gaussian with $\sigma = 500$ μm and $c = 0.5$, resulting in ∼ 50 connections from PCs to any PV cell (Strüber et al., 2017). Synapses from PV→PV were the same as for the PV ring network with varied peak conductance $\overline{g}_{\text{syn,PV}\to\text{PV}} \in \{1, 2, 4, 6, 8\}$ nS, and peak conductance $\overline{g}_{\text{syn,PV}\to\text{PC}} = 0.1$ mS/cm^2, corresponding to ∼ 0.5 nS for a typical dentate gyrus granule cell of size ∼ 500 μm^2 (Claiborne et al., 1990). PC→PV synapses have a peak conductance $\overline{g}_{\text{syn,PC}\to\text{PV}} = 2$ mS/cm^2 (Strüber et al., 2017) (for a parameter overview, see Figures S12A and S12B). Spike conductance delays had the same distance dependence for both PV basket cells and principal cells as for networks comprised only of PV basket cells.

Two-dimensional PV basket cell network

In addition to ring networks, we also created two-dimensional networks based on recent empirical data describing the distance dependence of the coupling probability between PV basket cells in the dentate gyrus (Espinoza et al., 2018) (for overview of network connectivity, see Figures S12A and S12B). It is given by the following equation and plotted in Figure S10C:

$$p_{\text{2dN}}(d) = \frac{1}{1 + \exp\left(\frac{d-a}{b}\right)} \qquad \text{(Equation 8)}$$

Here, we used $a = 50$ and $b = 115$ to approximately match the connection probability fit in (Espinoza et al., 2018). Notably, the spatial reach of connectivity is much smaller compared to the ring networks (Figures S10A and S10C), which means that assuming the same conduction velocity as used in ring networks, i.e., 0.25 m/s, the effective delays will be much shorter. Therefore, the effect of synchronized inhibition will be shortened, and oscillations will be faster. To compare synchrony in both network types in terms of network structure only, we thus assumed a three-times slower conduction velocity (0.0833 m/s) to match compound inhibition $G_{\text{GABA}}(t)$ in fully synchronous networks. Neurons were distributed uniform-randomly on a torus to avoid boundary effects.

External drive in anatomically detailed PV cell ring networks, ball-and-stick ring networks and 2D-networks

In most simulations, neurons were driven by Poisson-type excitatory synapses, that were distributed uniformly either perisomatically (<50 μm from the center of the soma) or on the outer two-thirds of the apical dendrites, i.e., >120 μm (>150 μm for ball-and-stick cells) from the soma center. The total input rate $r_{\text{stim}} = n_{\text{syn}} \times r$, where n_{syn} is the total number of synapses and r is the rate per synapse. We did not observe any qualitative or quantitative differences when varying n_{syn} or r while keeping r_{stim} fixed. Therefore, we decided to use $n_{\text{syn}} = 50$ for perisomatic, and $n_{\text{syn}} = 100$ for distal apical drive and varied r between 20 and 200 Hz.

External drive of network of PV basket cells and principal cells (PC)

PV basket cells and PCs were driven by Poisson-type excitatory synapses (''Exp2Syn''-synapses, see Figure S12B, where $\overline{g}_{\text{stim}\to\text{PC}} = 0.1$ mS/cm^2 corresponds to ∼ 0.5 nS for a typical dentate gyrus granule cell of size ∼ 500 μm^2 (Claiborne et al., 1990). Input rates were co-varied, such that input rates to PCs ranged from $r_{\text{stim,PC}} = 2000$–$7000$/s, and rate per synapse for PV basket cells was $r_{\text{stim,PC}}/40$ (100 synapses for dendritic stimulation, 50 synapses for perisomatic stimulation).

Theta-nested gamma oscillations

To simulate theta-modulated activity (Figure 5) we added a sinusoidally modulated current to the somatic compartment of all cells:

$$I_{\text{stim}}(t) = A \sin\left(\varphi + \frac{2\pi t}{T}\right) \qquad \text{(Equation 9)}$$

with oscillation period $f = 5$ Hz, and amplitude $A = 1$ nA. The phases φ were uniform-randomly sampled from $[0, \pi/2]$. Additionally, all cells received a heterogeneous amount of Poisson-type excitatory synaptic input as described above.

Simulation setup

Single cell simulations typically covered 2000 ms. For neurons driven with noisy or randomly distributed input we repeated the simulation ten times with different initial conditions for each parameter combination. Network simulations typically covered 500 ms. After

an initial period of 150 ms, the GABA-ergic synapses were activated. Some simulations (e.g., theta-nested gamma-oscillations) were run for 3000 ms to obtain sufficient data. Each network simulation was repeated at least 5 times with different random seeds per parameter combination to ensure different network structures, initial conditions, synapse locations and input spike trains. Exceptions are networks with gap junctions (Figure S4) and with shunting inhibition (Figures S5D–S5F where we only simulated one realization because they require very fine simulation steps to avoid numerical artifacts.

The simulation time step was chosen between $\delta t = 0.005$ ms (Figures S4 and S5D–S5F) and 0.025 ms (all other figures). All neurons and networks were simulated in NEURON/7.4 (Carnevale and Hines, 2006) via the pyNeuroML-interface (Vella et al., 2014) in NeuroML/v2beta4 (Cannon et al., 2014) (see Key resources table). Larger network simulations were run on the Sigma2 high-performance clusters Abel and Saga (https://www.sigma2.no). Versions of the models and simulation scripts are available online (see Key resources table). Data handling and analysis were done in Python/2.7.15, using the NumPy/1.11.9, SciPy/0.17.0, and Matplotlib/1.5.1 libraries (see Key resources table).

QUANTIFICATION AND STATISTICAL ANALYSIS

Gain of input-output (I-O) relationships

In Figure 1, we linearly interpolated the experimental I-O curves and determined the respective input current values $I_{10\%}, I_{70\%}$ at 10% and 70% of the maximal observed firing rate r_{max}. We then defined the gain as $\frac{0.6\ r_{max}}{(I_{70\%} - I_{10\%})}$. This captured the gain without being influenced by the saturating portion close to the maximum firing rate.

Spike rates

For analyzing single neuron simulations, we used the last 1500 ms or 2000 ms of simulated time, while for analyzing network simulations we used the last 300 ms or 500 ms (see Section "Simulation setup"). The spike detection threshold was 0 mV for the anatomically detailed- and "ball and sticks" PV basket cell model, and −20 mV for the principal cell (granule cell) model. Individual spike rates were computed as the number of spikes emitted by a neuron over the considered time interval T. Population spike rates were individual spike rates averaged across all neurons in a network.

The coefficient of variation of interspike intervals (ISI)

This is defined as the ISI standard deviation over the mean, i.e., CV(ISI) = σ(ISI)/μ(ISI).

Oscillation frequency

We computed the average membrane potential of all neurons and calculated its power spectrum using the function periodogram() from the scipy.signal module in the SciPy package. The frequency of the dominant peak then defined the oscillation frequency.

Synchrony Index

We first binned the spikes of all neurons that spiked at least two times in $\Delta = 2$ ms bins to obtain the spike histogram (Figure S13A). Next, we calculated the Fano Factor (FF) of the spike histogram, i.e.,

$$\mathrm{FF} = \frac{\sigma^2[\mathrm{count}]}{\mu[\mathrm{count}]}$$

$$\text{with} \quad \mathrm{count} = \mathrm{hist}\left[\sum_{i=1}^{N} X_i\right]$$

$$\text{with} \quad X_i = \mathrm{hist}[(S_i(t)|\Delta)],$$

$$\text{with spike trains} \quad S_i(t) = \sum_j \delta_j(t - t_j)$$

We then divided FF by the number of spiking neurons in the network. Thus, if all cells spike synchronously, the variance of the bin size will be maximal and FF/N equal to 1. If all cells spike asynchronously, the variance of the bin size will be minimal, and FF/N will approach 0. We excluded neurons that spiked less than two times in the considered time interval.

The maximal Synchrony Index per frequency band (see, e.g., Figure 3D) was determined as follows: first we averaged all parameter scans (five runs per parameter tuple ($\overline{g}_{\mathrm{syn,GABA}}$, total input rate) in Figures 3, 4, and 6) and determined the maximal Synchrony Index per frequency band. To obtain the error we computed the SEM across runs for the respective ($\overline{g}_{\mathrm{syn,GABA}}$, total input rate)-tuple of maximal Synchrony Index. For Figure 5 we only had one run covering 3000 ms of simulated time per parameter tuple. We chose

the last twelve theta-peaks of maximal network activity to compute the Synchrony Index, which was then averaged. The maximal Synchrony Index per frequency band respective SEM across theta-peaks is shown in Figure 5D.

To quantify network synchrony, previous work used the so-called Coherence Measure (Bartos et al., 2002; Vida et al., 2006; Wang and Buzsáki, 1996). To compare the Synchrony Index with the Coherence Measure, we plotted their relationship (Figure S13B). Note that both measures give very similar results. However, FF/N had several advantages: First, it does not have the floor effect that we observed for coherence-based measures (Figure S13B). Second, the Synchrony Index is simpler and infers the population-wide synchrony more directly because it is inherently a population-activity measure, whereas the Coherence Measures are based on pairwise synchrony.

Statistical analyses

Statistical details of experiments and simulations are provided in the figure legends and were performed in Python.

Cell Reports, Volume *39*

Supplemental information

Parvalbumin interneuron dendrites enhance gamma oscillations

Birgit Kriener, Hua Hu, and Koen Vervaeke

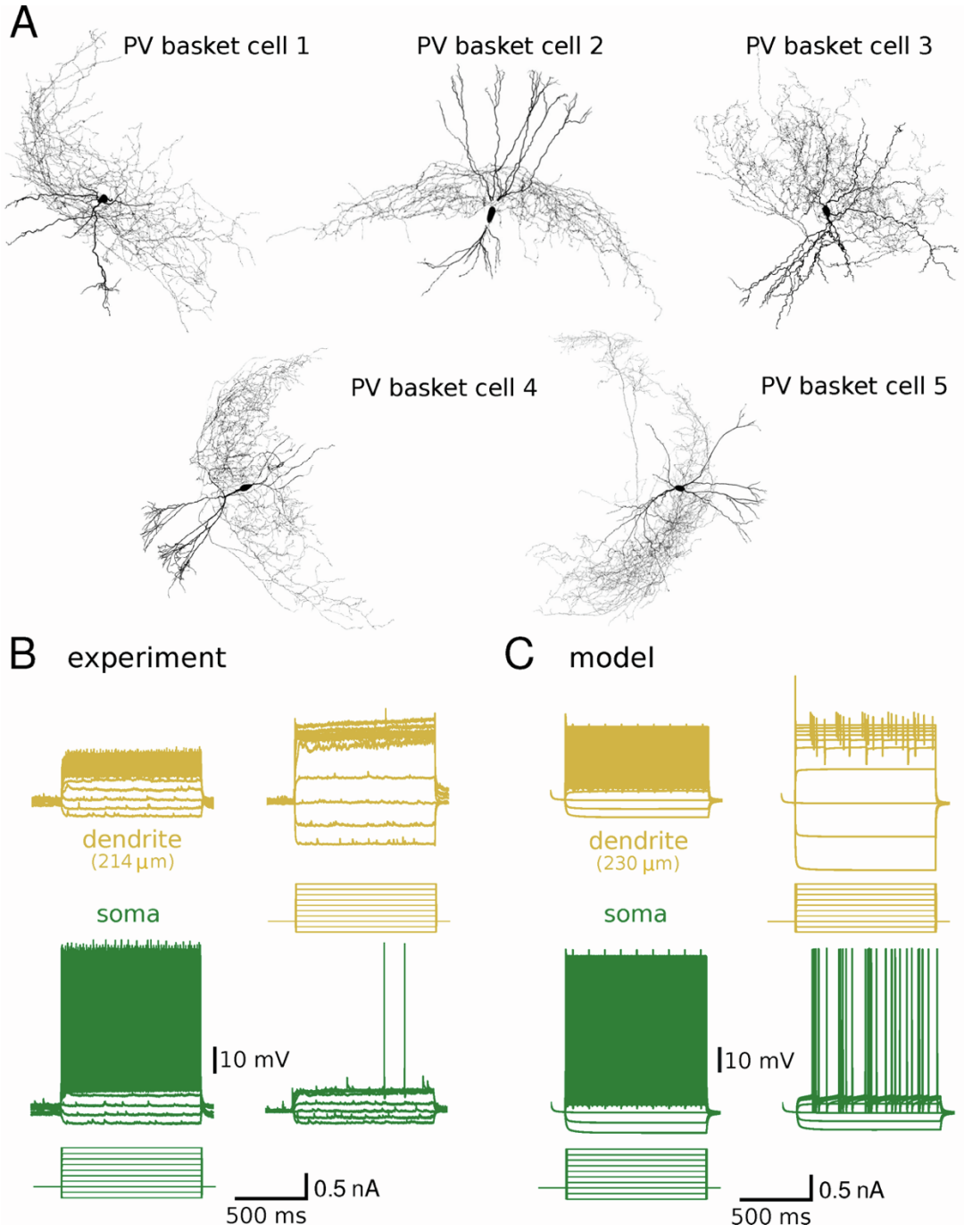

Figure S1. Morphology and physiological properties of the PV basket cell models. Related to Figure 1.

(A) Morphologies of five reconstructed parvalbumin (PV)-expressing basket cells in the rat dentate gyrus used for simulations (obtained from (Nörenberg et al., 2010)).

(B) Example of a dual soma-dendritic patch clamp recording. Voltage traces show soma and dendrite responses to current injections in either the soma (left) or the dendrite (right). Recording distance was 214 µm from the soma. Scale bars apply to soma and dendrite recordings.

(C) Same recording configuration as in (B). Model responses can be compared with experiments in (B). Model example is PV basket cell #2 (see (A), recording distance is 230 µm). Note that the fast transient at the onset of dendritic depolarization is a simulation artefact due to the instantaneous nature of the stimulus.

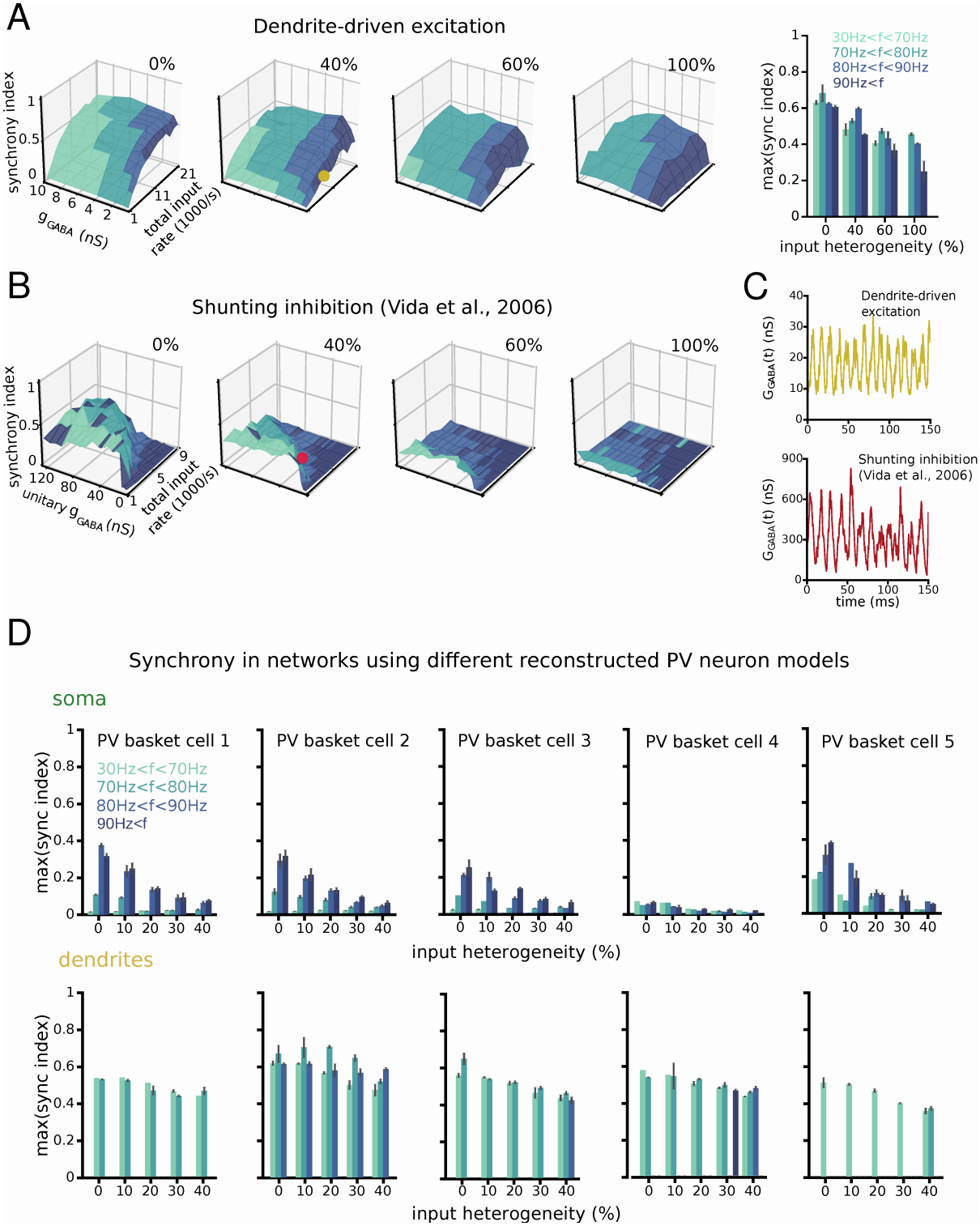

Figure S2. Robust dendrite-driven synchrony is maintained for high levels of input heterogeneity and is a property of all PV basket cell models tested. Related to Figure 3.

(A) 3D planes; Synchrony Index as a function of increasing input heterogeneity (0, 40, 60, 100 %). Right, histogram of the maximum Synchrony Index per frequency band, as a function of input heterogeneity. Mean ± SEM, 5 network instantiations.

(B) Synchrony Index of a previously published landmark model using single compartment cells and shunting inhibition (Vida et al., 2006). Same levels of heterogeneity as in (A).

(C) Comparison of the total inhibitory synaptic conductance that is received by a single PV basket cell, using either the dendrite-driven model (top) or the shunting inhibition model. The traces correspond to the orange and red dots on the 3D planes in (A) and (B). Note that we chose the network parameters with the lowest g_{GABA} that still produced synchrony.

(D) Comparison of network simulations using the five different PV basket cell models. Histograms show the maximum Synchrony Index per frequency band, as a function of input heterogeneity. Mean ± SEM, 5 network instantiations.

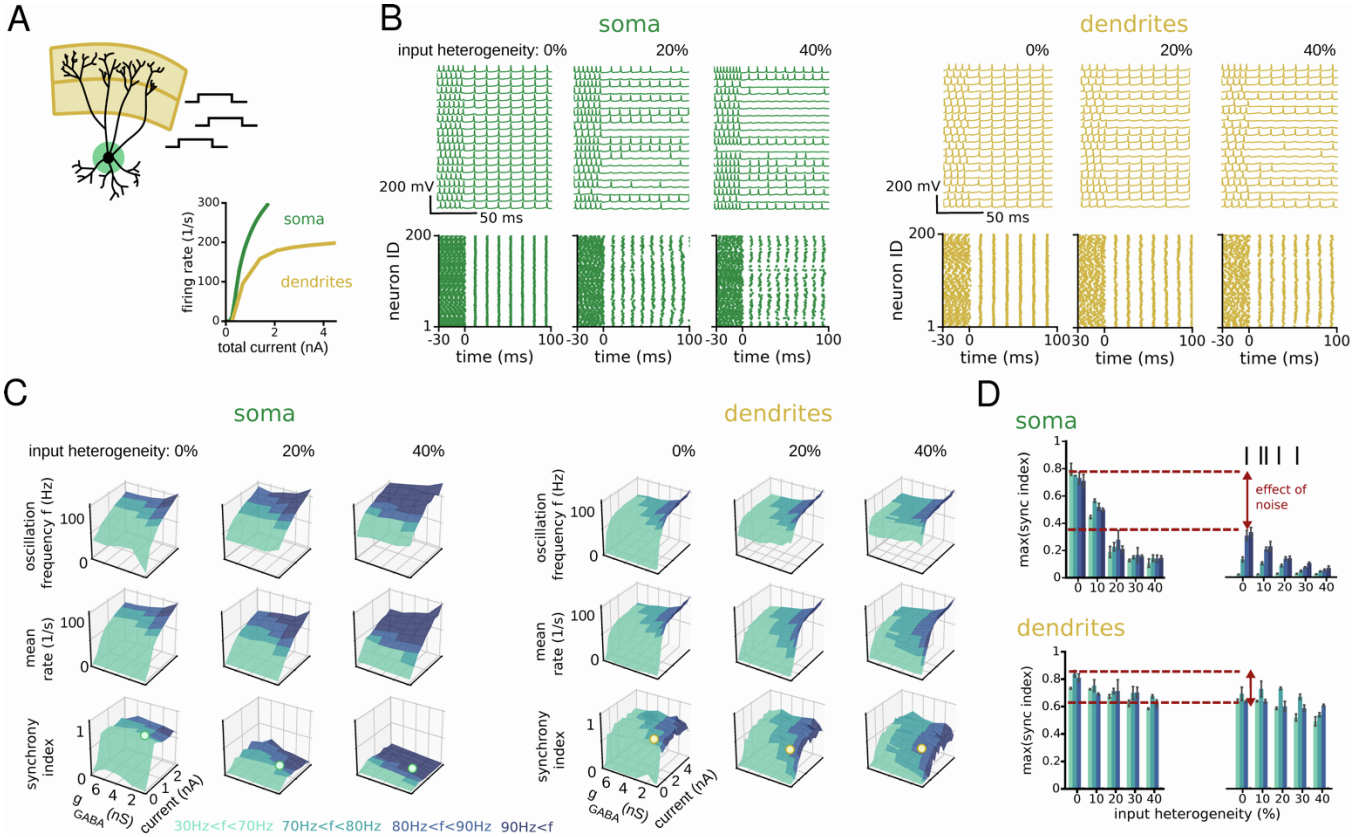

Figure S3. Noisy synaptic input is an important determinant of network synchrony. Related to Figure 3.

(A) Cartoon illustrating a PV basket cell model driven by noiseless direct current (DC) inputs, distributed either perisomatically (green, 50 inputs ≤ 50μm from the soma), or on the dendrites (orange, 100 inputs ≥ 120μm from the soma). Bottom panel shows I-O relationships using either perisomatic or dendritic DC input.

(B) PV basket cell activity in ring networks consisting of 200 PV basket cells driven by perisomatic (green) or dendritic (orange) excitation. Input heterogeneity increases from left to right. Top row, example membrane potential traces showing spikes from 20 random cells. Bottom row, raster plots of all 200 PV basket cells in the network. Network starts uncoupled and inhibitory synapses activate at t=0 ms.

(C) Network oscillation frequency (top row), average spike rate (middle row) and Synchrony Index (bottom row) as a function of total input rate and the strength of unitary inhibitory connections (gGABA). Colour legend shows the oscillation frequency ranges. The dots on the 3D planes of the Synchrony Index correspond to the examples in (B).

(D) The maximum Synchrony Index per frequency band, as a function of input heterogeneity for perisomatc and dendritic input (based on data in (B) and (C)). The Synchrony Index is shown for DC inputs (left panels) and for Poisson trains of synaptic conductances (right panels). Mean ± SEM, 5 network instantiations.

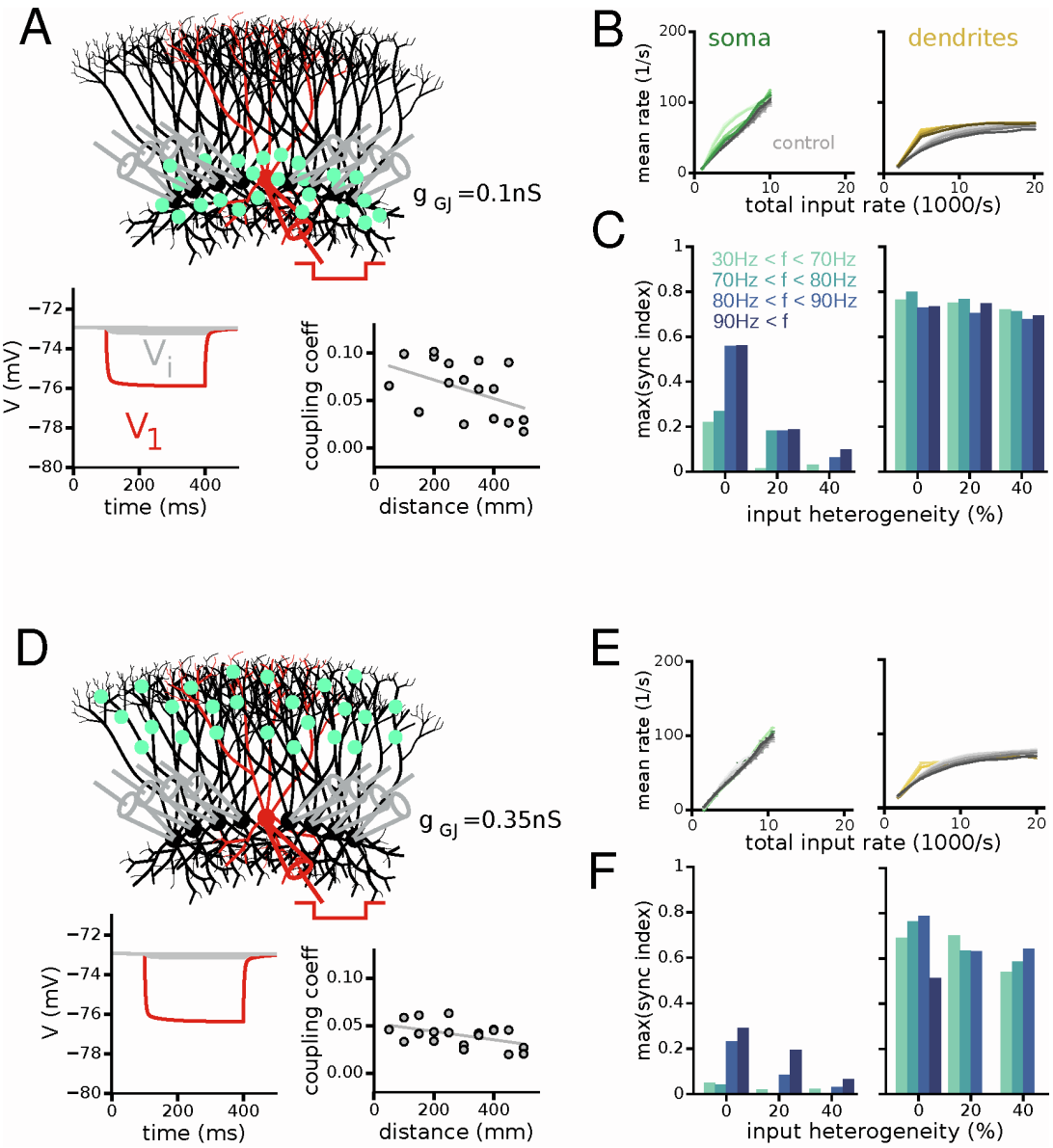

Figure S4. Enhanced robustness of dendrite-driven synchrony does not depend on electrical synapses. Related to Figure 3.

(A) Network simulations of PV basket cells connected with electrical synapses located in the perisomatic area, in addition to chemical inhibitory synapses. Cartoon of the recording configuration to test electrical coupling strength between two nearby PV basket cells. Electrical synapses are inserted on the soma and proximal dendrites (≤ 50 μm, individual conductance g_{GJ} = 0.1 nS) (see Methods). Bottom left; membrane potential responses of PV basket cells in a fully coupled network in response to a current pulse (-0.1 nA) in one of the cells (red). Bottom right; Electrical coupling strength is defined by the Coupling Coefficient (CC; the ratio of voltage changes in the cell pair, V2/V1x100). Coupling coefficient is shown as a function of distance between somata.

(B) I-O relationships showing the mean spike rate of all PV basket cells in the network. This graph corresponds to a slice along the y-axis of the 3D plots as in Fig.3C for gGABA = 4 nS. Left, soma-driven networks. Right, dendrite-driven networks. Light to dark grey lines: increasing heterogeneity (0, 10, 20, 30, 40 %) for networks

without electrical synapses (control). Light to dark coloured lines, increasing heterogeneity for networks that also include electrical synapses. Mean ± SEM, 1 network instantiation.

(C) The maximum Synchrony Index per frequency band, as a function of input heterogeneity. Left, soma-driven networks. Right, dendrite-driven networks. Mean ± SEM, 1 network instantiation.

(D-F) Same as (A-C) but electrical synapses are located only on the dendrites (>120 μm from the soma, individual conductance $g_{GJ} = 0.35$ nS).

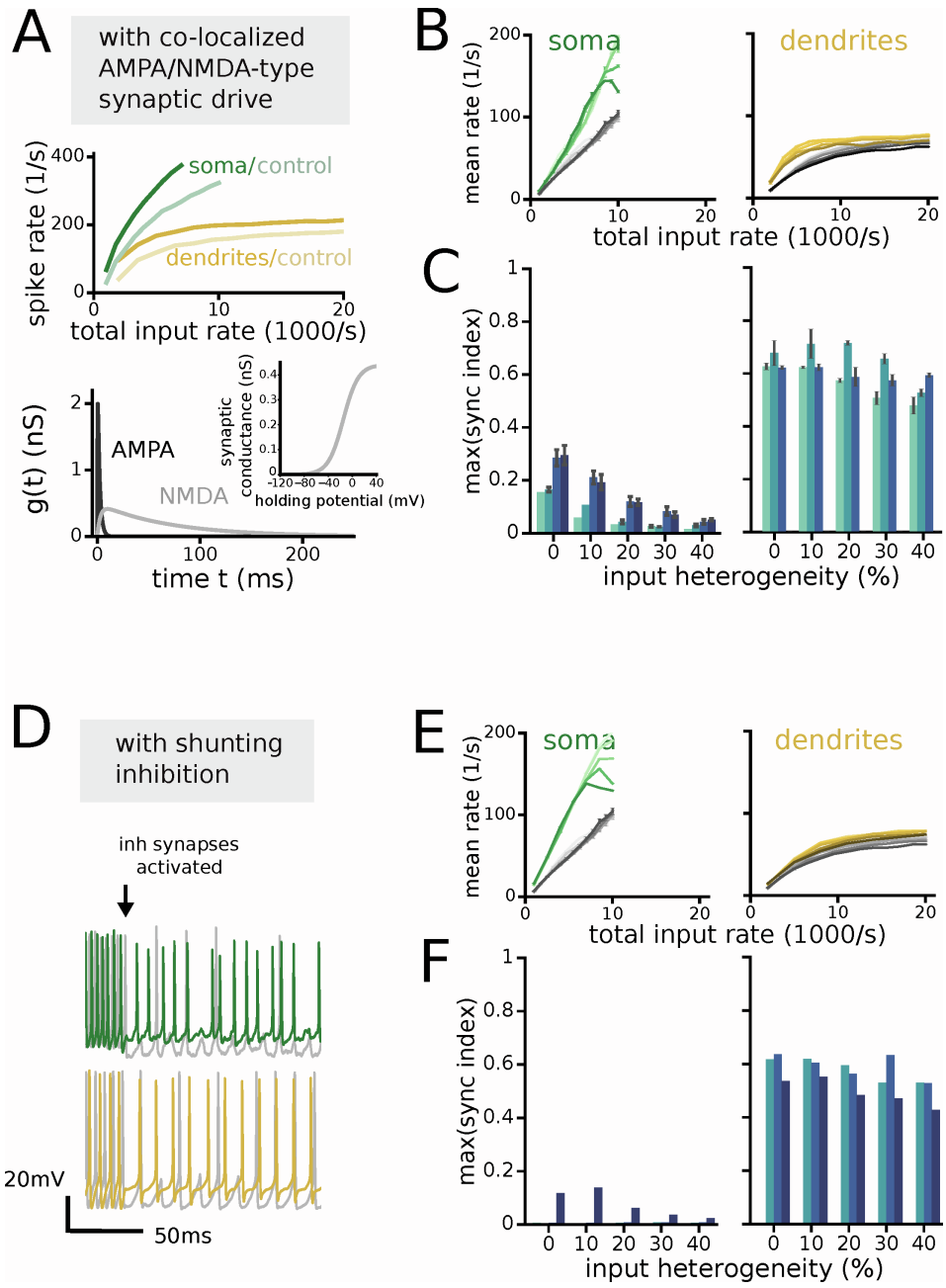

Figure S5. Enhanced robustness of dendrite-driven synchrony does not depend on NMDA receptors or shunting inhibition. Related to Figure 3.

(A-C) Simulations of PV basket cell networks with co-localized AMPA and NMDA receptors.

(A) Top, I-O relationships of a PV basket cell model, driven by excitatory input either close to the soma or on the dendrites. Faint curves are I-O relationships with only AMPA receptors. Bottom, kinetics and conductance of AMPA and NMDA receptors. The maximum conductance ratio between NMDA (0.42 nS) and AMPA receptors (2 nS) is ~0.21 (see (Koh et al., 1995)). Inset, voltage dependence of the NMDA receptors.

(B) I-O relationships showing the mean spike rate of all PV basket cells in the network. This graph corresponds to a slice along the y-axis of the 3D plots as in Figure 3C for gGABA = 4nS. Left, soma-driven networks. Right, dendrite-driven networks. Light to dark grey lines: increasing heterogeneity (0, 10, 20, 30, 40%) for networks

without NMDA synapses (control). Light to dark coloured lines, increasing heterogeneity for networks that also include NMDA synapses. Mean ± SEM, 5 network instantiations.

(C) The maximum Synchrony Index per frequency band, as a function of input heterogeneity. Left, soma-driven networks. Right, dendrite-driven networks. Mean ± SEM, 5 network instantiations.

(D-F) Network simulations of PV basket cells with shunting inhibition.

(D) Example voltage traces of PV basket cells in a ring network with shunting inhibitory connections. Grey, simulation with hyperpolarizing inhibition. Green, soma-driven networks with shunting inhibition; Orange, dendrite-driven networks with shunting inhibition. The resting potential is -73 mV (in the absence of any input), reversal potential of hyperpolarizing inhibition is -75 mV and for shunting inhibition -60 mV.

(E, F) Same as (B,C) but for networks with shunting inhibition. Mean ± SEM, 1 network instantiation.

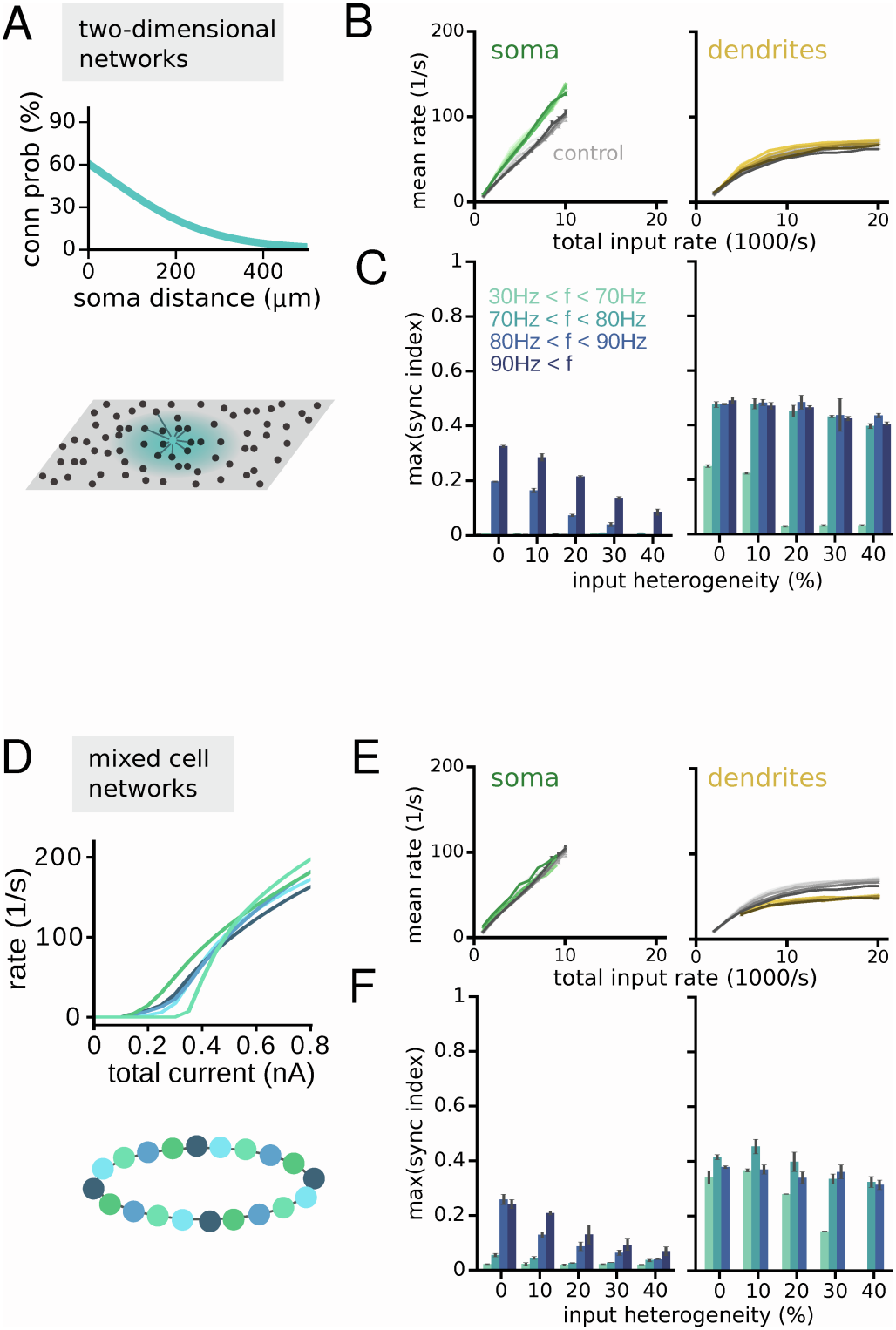

Figure S6. Enhanced robustness of dendrite-driven synchrony is maintained in PV basket cell networks with a 2D organization and in mixed PV basket cell networks. Related to Figure 3.

(A-C) Simulations using PV basket cell networks with a 2D organization. PV basket cells were arranged on a 2D torus (see Methods).

(A) Connection probability of PV basket cells as a function of distance between their somata. Adapted from experimental data on PV basket cells in the dentate gyrus reported in (Espinoza et al., 2018). Bottom, cartoon showing a 2D patch of PV basket cells with local spatial connectivity.

(B) I-O relationships showing the mean spike rate of all PV basket cells in the network (this graph corresponds to a slice along the y-axis of the 3D plots as in Figure 3C for gGABA = 4 nS). Left, somatic-driven networks (50 synapses ≤ 50μm from the soma). Right, dendrite-driven networks (100 synapses ≥ 120μm from the soma). Light to dark grey lines: increasing heterogeneity (0, 10, 20, 30, 40%) for ring networks with local connectivity (control). Light to dark coloured lines, increasing heterogeneity for networks with random spatial connectivity. Most I-O relationships overlap. Mean ± SEM, 3 network instantiations.

(C) The maximum Synchrony Index per frequency band as a function of input heterogeneity. Left, soma-driven networks. Right, dendrite-driven networks. Mean ± SEM, 3 network instantiations.

(D-F) Simulations using networks consisting of a mix of all five PV basket cell models with a reconstructed morphology (see Methods).

(D) Top, I-O relationships of all five PV basket cell models. Bottom, cartoon illustrating a ring network consisting of a mix of five different PV basket cell models.

(E,F) Same as (B,C) for mixed PV basket cell networks.

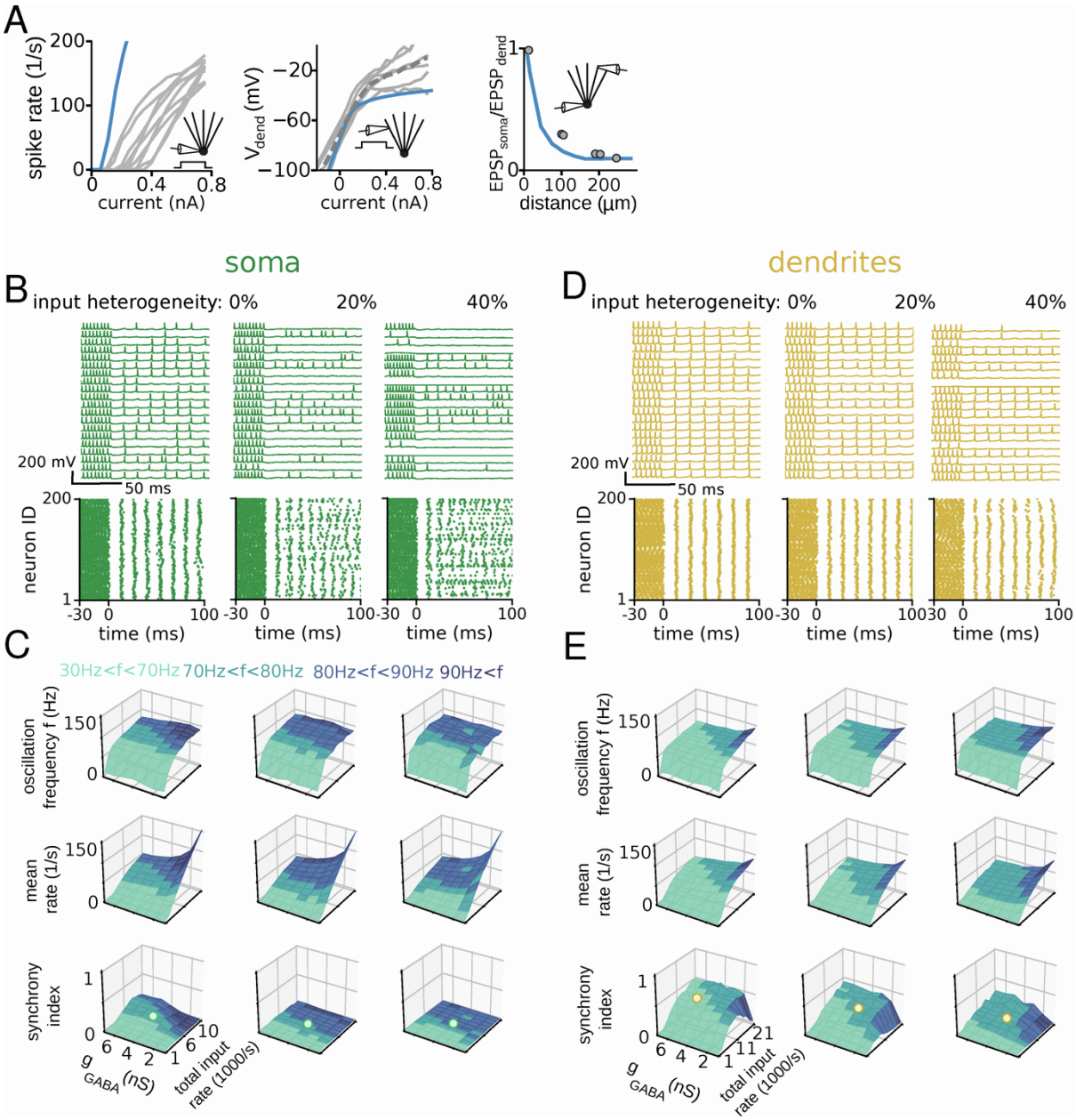

Figure S7. A simplified PV basket cell model approximates the biophysical and network properties of the detailed PV basket cell models. Related to Figure 4.

(A) Comparison of the biophysical properties of the simplified model (blue) and the experimental data (grey, same experimental data as in Figure 1 and 2). Left, I-O relationship when injecting current steps in the soma. Middle, V-I relationship when injecting current steps in the dendrite. Dendritic recording distance is 230 μm from the soma. Right, attenuation of the EPSP amplitude during propagation from the dendrites to the soma.

(B) PV basket cell activity in the network driven by perisomatic excitation. Input heterogeneity increases from left to right. Top, example membrane potential traces from 20 random PV basket cells. Bottom, raster plots of all 200 cells in the network. Network starts uncoupled and inhibitory synapses activate at t=0 ms.

(C) Characterization of soma-driven networks as a function of input heterogeneity. Top, network oscillation frequency. Middle, average spike rate. Bottom, Synchrony Index. All are shown as a function of total input rate

and inhibitory synaptic conductance. Colour legend indicates the oscillation frequency bands. White dots on the Synchrony Index correspond to the data in (B).

(D) As in (B), but for PV basket cell networks driven with dendritic input (100 synapses ≥ 150 μm from the soma).

(E) As in (C), but for PV basket cell networks driven with dendritic input.

A

Passive parameters					
Cell	**PV1**	**PV2**	**PV3**	**PV4**	**PV5**
C_m [$\mu F/cm^2$]	0.99	1.06	0.77	0.92	0.97
R_i [Ωcm]	149	137	141	178	258
E_{leak} [mV]	-80	-73	-80	-75	-75

B

g_{leak} [mS/cm^2]					
Cell	**Soma**	**Proximal Dendrites** ($< 120\mu m$)	**Distal Dendrites** ($\geq 120\mu m$)	**Proximal Axon** ($< 120\mu m$)	**Distal Axon** ($\geq 120\mu m$)
PV1	0.157	0.157	0.079	0.003	0.003
PV2	0.157	0.157	0.079	0.003	0.003
PV3	0.1	0.1	0.05	0.0014	0.0014
PV4	0.2	0.2	0.048	0.007	0.007
PV5	0.093	0.093	0.065	0.0037	0.0037

C

Active Channel Parameters	
E_{Na} [mV]	55
ϕ_{Na}	5
E_{K1} [mV]	-90
ϕ_{K1}	2 (5 for Ball-and-stick model)
E_{K2} [mV]	-90
ϕ_{K2}	5

D

Active Channel Densities					
Densities [mS/cm^2]	**Soma**	**Proximal Dendrites**	**Distal Dendrites**	**Proximal Axon**	**Distal Axon**
PV1					
g_{Na}	100	5	5	400	35 ($>120\mu m$)
g_{K1}	40	40	0 ($>200\mu m$)	40	40
g_{K2}	0	0	30 ($>200\mu m$)	0	0
PV2					
g_{Na}	250	5	5	550	35 ($> 120\mu m$)
g_{K1}	50	50	0 ($>200\mu m$)	50	50
g_{K2}	0	0	30 ($>200\mu m$)	0	0
PV3					
g_{Na}	200	5	5	400	35 ($>120\mu m$)
g_{K1}	50	50	0 ($>200\mu m$)	50	50
g_{K2}	0	0	30 ($>200\mu m$)	0	0
PV4					
g_{Na}	120	5	5	400	35 ($>120\mu m$)
g_{K1}	60	60	0 ($>200\mu m$)	60	60
g_{K2}	0	0	30 ($>200\mu m$)	0	0
PV5					
g_{Na}	150	5	5	450	35 ($>120\mu m$)
g_{K1}	50	50	0 ($>200\mu m$)	50	50
g_{K2}	0	0	30 ($>200\mu m$)	0	0

E

Input Resistance					
Cell	**PV1**	**PV2**	**PV3**	**PV4**	**PV5**
R_{inp} [$M\Omega$] exp	119.2	57.3	118.8	63.4	60.7
R_{inp} [$M\Omega$] model	97.5	63.1	108.3	48.7	64.5

Figure S8. Model parameters. Related to STAR Methods. (A) Passive parameters of the detailed PV basket cell models (Adapted from Nörenberg et al. (2010)). **(B)** Leak conductances of the detailed PV basket cell models (Adapted from Hu et al. (2010) and Nörenberg et al. (2010)). **(C)** Parameters of the voltage-dependent ion channels. **(D)** Fitted parameters of the voltage-dependent ion channels of the detailed PV basket cell models: Current density of I_{Na} and the two potassium channels I_{K1} and I_{K2}. **(E)** Comparison of input resistance between experimental data (Nörenberg et al. (2010)) and cell models.

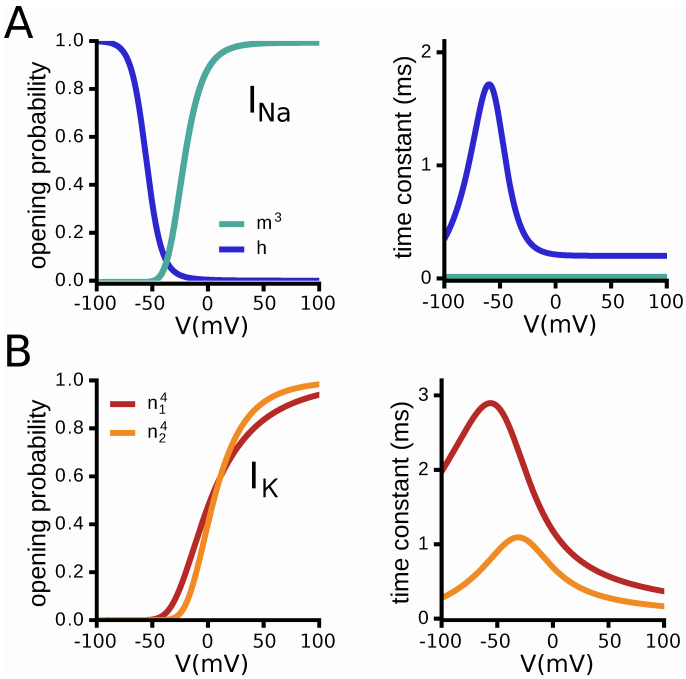

Figure S9. Voltage-dependent steady-state activation and inactivation curves and time constants of I_{Na} and I_{K1}, I_{K2}. Related to STAR Methods. Left side: Steady state activation of the **(A)** activation variable m^3 and inactivation variable h of the sodium channel, and **(B)** of the activation variables $n1$, $n2$ of the potassium channels. Right side: respective time constants.

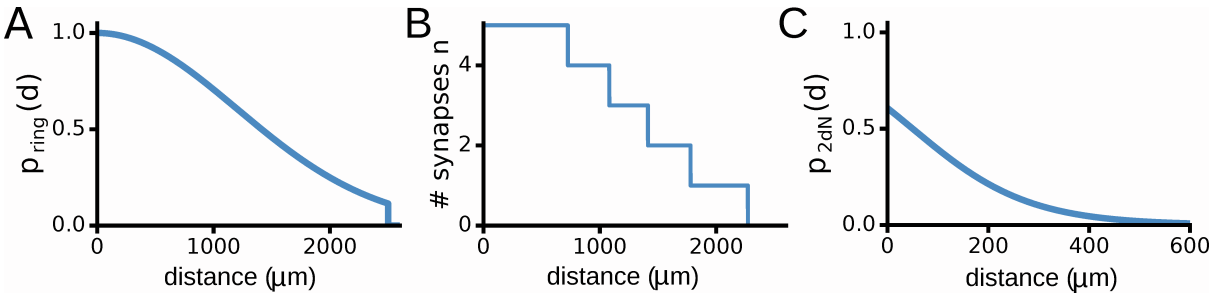

Figure S10. Network connectivity. Related to STAR Methods. (A) Connection probability of PV basket cells in the ring networks. **(B)** Number of synaptic contacts between PV baskets cells as a function of distance between cells. **(C)** Connection probability of PV basket cells in the 2D network (adapted from Espinoza et al. (2018)).

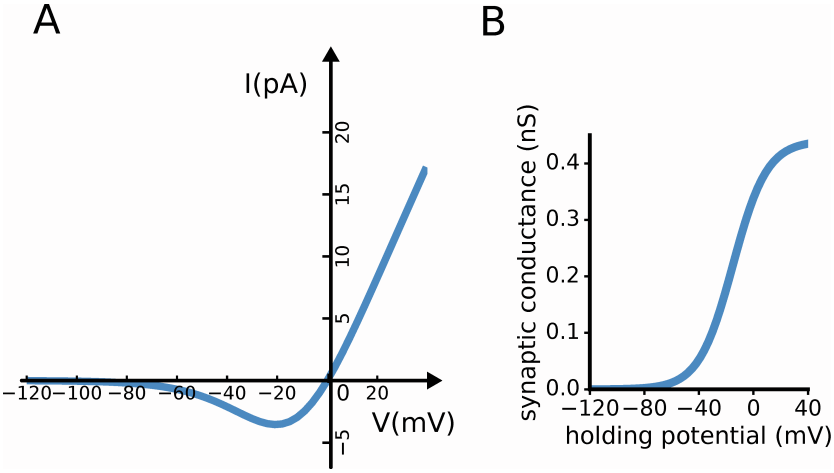

Figure S11. NMDA conductance properties. Related to STAR Methods. (A) I-V-relationship of the NMDA conductance. **(B)** Voltage dependence of the NMDA conductance.

A

Synaptic Parameters				
Synapse Type	τ_{syn}^{rise} **[ms]**	τ_{syn}^{decay} **[ms]**	$\bar{g}$ **[nS]**	E_{rev} **[mV]**
PV→PV (GABA)	0.16	1.8	0.5-10	−75 (hyperpol), −60 (shunting)
Ext→PV (AMPA)	0.2	2	2	0
Ext→PV (NMDA)	3	70	0.44	0
PV→PC (GABA)	0.16	7	0.1	−65
PC→PV (AMPA)	0.1	1	2	0
Ext→PC (AMPA)	0.1	1	0.1	0

B

Network Specifications					
Network Type	**Dimension**	**Metric**	**Boundary Condition**	**Cell Distribution**	**Connectivity Profile**
ring network	one	absolute difference	periodic	equilateral grid	boxcar $p(d) = \Theta[d_{max} - d]$
random network	two	euclidean	periodic	uniform random	sigmoid $p(d) = \frac{1}{1+\exp\left(\frac{d-a}{b}\right)}$

Figure S12. Synaptic and network connectivity parameters. Related to STAR Methods. (A) Parameters of "Exp2Syn"-synapses. **(B)** Specifications of network models.

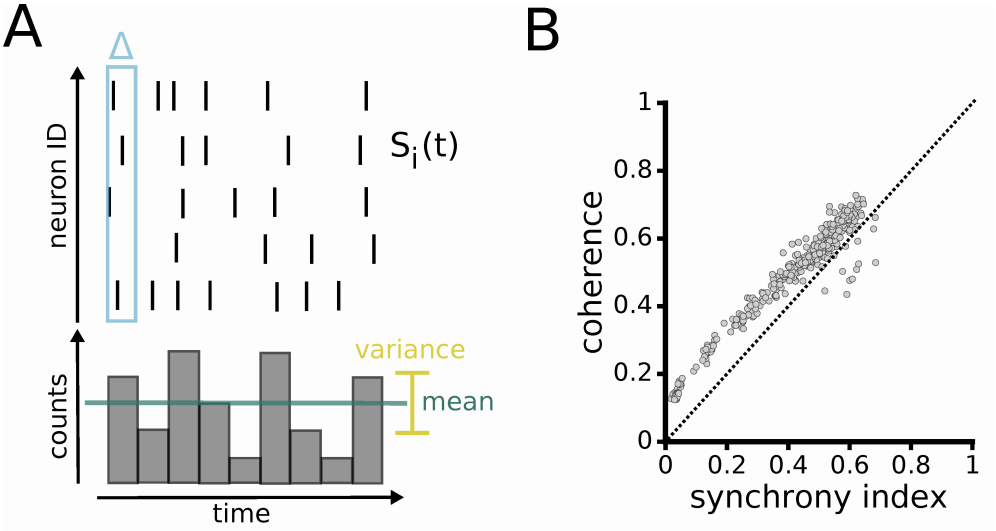

Figure S13. Fano Factor measures population wide synchrony. Related to STAR Methods. (A) Cartoon showing how the Synchrony Index is computed. Upper panel: spike raster plot. Lower panel: population spike count histogram. **(B)** Example scatter plot of the relationship between Synchrony Index and Coherence.